



ARTICLE

## A Fractional-Order Machine Learning Framework for Modeling Vertebral Column Pathology and Biomechanical Dynamics

David Amilo<sup>1,\*</sup>, Khadijeh Sadri<sup>1</sup>, Evren Hincal<sup>1,2</sup>, Chinedu Izuchukwu<sup>3</sup>, Mohamed Hafez<sup>4,5</sup>,  
Muhammad Farman<sup>1,6,7</sup> and Kottakkaran Soopy Nisar<sup>8,9</sup>

<sup>1</sup>Mathematics Research Center, Near East University TRNC, Mersin 10, Nicosia, Turkey

<sup>2</sup>Research Center of Applied Mathematics, Khazar University, Baku, Azerbaijan

<sup>3</sup>School of Mathematics, University of the Witwatersrand, Private Bag 3, Johannesburg, South Africa

<sup>4</sup>Department of Civil Engineering, Faculty of Engineering, FEQS INTI-IU, University, Nilai, Malaysia

<sup>5</sup>Faculty of Management, Shinawatra University, Pathum, Thani, Thailand

<sup>6</sup>Department of Computer Engineering, Biruni University, Istanbul, Turkey

<sup>7</sup>International Center for Interdisciplinary Research in Sciences, The University of Lahore, Lahore, Pakistan

<sup>8</sup>Department of Mathematics, College of Science and Humanities in Alkharj, Prince Sattam Bin Abdulaziz University, Alkharj, Saudi Arabia

<sup>9</sup>Hourani Center for Applied Scientific Research, Al-Ahliyya Amman University, Amman, Jordan

\*Corresponding Author: David Amilo. Email: [amilodavid.ikechukwu@neu.edu.tr](mailto:amilodavid.ikechukwu@neu.edu.tr)

Received: 19 December 2025; Accepted: 16 March 2026; Published: 30 June 2026

**ABSTRACT:** Spinal disorders, such as disk hernia and spondylolisthesis, affect millions worldwide, leading to chronic pain and reduced quality of life due to disruptions in biomechanical alignment. Traditional diagnostic methods often overlook the viscoelastic memory effects in spinal tissues, necessitating advanced models that integrate machine learning with fractional calculus for improved accuracy and interpretability. The research introduces a new fractional-order machine learning system that analyzes vertebral column abnormalities through biomechanical motion analysis by using the University of California, Irvine (UCI) vertebral column dataset. The system selects the best machine learning model from Random Forest (RF), Gradient Boost (GB), XGBoost, Deep Neural Network (DNN), and Voting Ensemble (VE) models to work with Caputo fractional-order differential equations, which simulate spinal tissue viscoelasticity memory effects through pseudo-time analysis of pelvic incidence data. The study demonstrates that GB achieves its highest accuracy at 0.937, and RF attains its top Area Under the Curve (AUC) at 0.949, and the fractional model achieves a weighted Mean Squared Error (MSE) of 0.0017. The optimized parameters showed that the growth rates and coupling coefficients worked in an inhibitory manner. The biological findings demonstrated that patients with higher pelvic incidence and lumbar lordosis variability experienced greater spinal stress, which led to compensatory curvature patterns that: disk hernia and spondylolisthesis development. The results showed that pelvic incidence and sacral slope had the strongest correlation at 0.87, and pelvic incidence and lumbar lordosis angle showed a correlation of 0.74, which informs the fractional-order growth rates where higher-correlated features evolve faster under pathological stress due to their mechanical interdependence. Theoretical proofs establish solution existence and uniqueness and boundedness, and stability, and numerical efficiency emerges from the Adams-Bashforth-Moulton method, while a diagnostic Graphic User Interface (GUI) enables clinical application. The framework enables better spinal disease detection through fractional derivatives, which replicate real biomechanical operations.

**KEYWORDS:** Machine learning; fractional calculus; spinal pathology; biomechanical dynamics; public health; preventable deaths

## 1 Introduction

The human spinal column functions as the core structure of the skeleton while providing movement abilities and stability and safeguarding the spinal cord through its network of 33 vertebrae and intervertebral discs, and ligaments [1–5]. The natural balance between vertebral bones and discs becomes disrupted by spinal conditions like disk hernia and spondylolisthesis, which lead to persistent pain and functional decline that affects more than 80% of adults during their lifetime [6–8]. The conditions produce changes in biomechanical measurements, which include pelvic incidence and lumbar lordosis angle and sacral slope, pelvic tilt, and pelvic radius, because these measurements show how the spine is aligned and how weight is spread out [9–12]. The diagnosis process needs immediate treatment, but current methods fail to detect the intricate and memory-based spinal biomechanics. Conventional diagnostic methods depend on imaging techniques, which include X-rays and CT scans, and Magnetic Resonance Imaging (MRI), together with statistical models to detect structural defects [13–15]. Research shows that pelvic incidence determines spinal alignment through its direct relationship with lumbar lordosis and sacral slope measurements in people who have normal spinal structure [16–18]. Authors of [19] developed and evaluated an artificial intelligence algorithm to automate vertebral column segmentation in biplanar full-body radiographic images for degenerative scoliosis (DS) assessment. The research used 250 anonymous high-definition X-ray images from an institutional Picture Archiving and Communication System (PACS) to train and test a two-stage deep learning model based on U-Net (UNET) architecture, which included 200 images for training and 50 images for evaluation. The model first identified the spine region in full-body X-rays and then isolated spinal curvature, achieving high accuracy with Dice-Sørensen coefficients of 0.92 for anterior-posterior and 0.96 for lateral views, even in cases with complex spinal pathologies like lordosis, scoliosis, and spinal instrumentation. The researchers used a cross-sectional study [20] to study how spinopelvic alignment varies while creating a spinal balance classification system and developing formulas to predict lumbar lordosis (LL) based on pelvic incidence (PI). Sagittal parameters were evaluated using radiographic assessments, and participants were grouped into three distinct clusters with varying PI and LL averages using K-means clustering and a decision tree incorporating PI and sacral slope (SS). The prediction of LL and SS through cluster-specific linear regression models produced moderate correlation results. The authors of [21] studied how pelvic biomechanics, including pelvic incidence (PI) and pelvic tilt (PT) and lumbar lordosis (LL) and sacral slope (SS), and pelvic radius (PR), might predict spinal disorders like scoliosis and spondylolisthesis. Data from a centralized orthopedic database were used, with spine conditions classified as normal or abnormal based on imaging and clinical exams. Descriptive statistics, comparative analyses, decision trees, and logistic regression identified PI, LL, SS, and PR as significant predictors, with decision trees accurately classifying 69.5% of cases based on PI thresholds and models validated via ROC analysis and 10-fold cross-validation. The research identified abnormal sagittal spinopelvic alignment as the main cause of improper spinal load distribution while showing that higher Body Mass Index (BMI) increases the chance of developing degenerative central stenosis. The research shows how pelvic parameters lead to spinal problems, which creates new possibilities for better diagnostic methods and individualized treatment plans, yet additional forward-looking research needs to enhance current prediction systems and study movement-based evaluations. The methods described above treat biomechanical features as unchanging elements because they fail to consider the viscoelastic nature of spinal tissues, which results in previous stresses affecting present behavior. The first biomechanical studies used integer-order differential equation models, which failed to consider the delayed responses of intervertebral discs and ligaments because these models do not include memory effects, as fractional-order models do [22–24]. The method shows its greatest weakness when modeling spondylolisthesis because it fails to capture the body's natural compensatory response, which results in increased lumbar lordosis.

Mathematical modeling has been instrumental in analyzing a wide range of phenomena with practical applications [25,26], where fractional-order calculus provides an effective way to solve these problems. The Caputo fractional derivative enables non-local memory-dependent system behavior, which scientists demonstrate through their work in biomechanical systems [27,28]. Fractional-order differential equations (FDEs) have been used to model viscoelastic tissues in other contexts, such as cartilage [29,30] and several other biological phenomena [31–33], but their application to spinal biomechanics remains underexplored. Medical diagnostics underwent a complete transformation through the use of machine learning (ML), which emerged as a leading innovation in healthcare [34,35]. Random Forest, Gradient Boost, XGBoost, and Deep Neural Networks have shown great promise for binary classification of abnormalities [36–38]. These models function well to detect patterns in large datasets, yet they struggle to provide explanations based on biomechanical principles. Studies about medical diagnostics show that Voting Ensembles enhance system stability through their use of ensemble methods [39–41]. Standalone ML methods do not include temporal information or tissue memory, which prevents them from effectively modeling disease progression.

Recent studies show that physics-informed neural networks, which combine ML with dynamic modeling through data-driven predictions and physical constraints, show promising results [42–44]. Yet, no prior work has fully bridged ML with fractional-order modeling for vertebral column pathology. The UCI vertebral column dataset contains 310 cases with six biomechanical features, which makes it an ideal resource for studying linked anatomical patterns between pelvic incidence and pelvic tilt and sacral slope as reported in clinical research.

The research presents an innovative fractional-order machine learning system that demonstrates the ability to model spinal conditions and biomechanical operations of the vertebral column. The system will use advanced ML algorithms to solve five linked Caputo FDEs, which will model tissue memory behavior and forecast abnormality probabilities. The idea of integrating ML algorithms with FDE models has recently been applied to some other biological phenomena and has proven quite positive [45–47]. The current framework processes the UCI dataset through Synthetic Minority Over-sampling Technique (SMOTE) oversampling and Z-score normalization, and Minimum Redundancy Maximum Relevance (MRMR) feature selection to identify pelvic incidence as a key feature. A diagnostic GUI system enables doctors to apply their findings in real-world clinical situations. The research uses an interdisciplinary approach that builds on existing studies to create a dynamic and interpretable system for spinal pathology diagnosis while showing potential for improved musculoskeletal health precision medicine. The rest of the paper is organized as follows: [Section 2](#) presents the methodology that integrates the ML algorithm and the FDE modeling. [Section 3](#) summarizes the data and data processing technique used. The ML algorithms are detailed in [Section 4](#). The developed FDE model, informed by the ML best-performing model, is presented in [Section 5](#), and its theoretical analysis is rigorously established in [Section 6](#). The numerical analysis is detailed in [Section 7](#), while the entire results and conclusion are presented in [Sections 8 and 9](#), respectively.

## 2 Methodology

The research methodology combines machine learning techniques with fractional-order differential equations to analyze vertebral column abnormalities through the UCI vertebral column dataset, which contains 310 samples with six biomechanical measurements and two class labels that include 210 abnormal and 100 normal cases. The dataset underwent preprocessing through SMOTE oversampling, which created 1000 instances to address class imbalance, and then Z-score normalization was used for standardization. The MRMR feature selection process identified five important features, which include pelvic incidence and lumbar lordosis angle, pelvic radius and sacral slope, and pelvic tilt. The fractional-order model received input features that were min-max scaled between 0 and 1. The evaluation process involved training

multiple machine learning models which included Random Forest with 500 trees minimizing Gini impurity and Gradient Boost with 300 trees at a learning rate of 0.02 minimizing exponential loss and XGBoost Approximate with 300 trees at the same learning rate minimizing logistic loss and DNN with cross-entropy loss and Rectified Linear Unit (ReLU) activation and 128/64 neuron layers and batch normalization and dropout rates of 0.3 and 0.2 optimized through Adam and Voting Ensemble that combined these models with logistic regression using majority voting. The models underwent evaluation through 10-fold cross-validation, which measured their performance by accuracy, precision, recall, F1 score, AUC, and computation time. The model consists of five interconnected Caputo fractional differential equations, which operate at an order of 0.8 to represent normalized biomechanical features, pelvic incidence, pelvic tilt, lumbar lordosis angle, sacral slope, and pelvic radius. Their correlations directly influence the fractional-order growth rates in the model, with strongly linked parameters exhibiting accelerated evolution under stress, reflecting how pathological changes in one propagate to others via viscoelastic tissue responses. The model uses logistic growth functions to simulate bounded systems and linear relationships to represent mechanical connections between body parts. The model uses logistic growth functions to represent bounded systems and linear relationships between body parts to simulate their mechanical interactions. The sum of pelvic tilt and sacral slope creates the approximation for pelvic incidence. The model uses pseudo-time, which orders patients based on their pelvic incidence measurements to show how their disease progresses. The Caputo fractional derivative models viscoelastic memory effects in spinal tissues based on the best-performing ML model shown in Fig. 1. The system was solved numerically using the Adams-Bashforth-Moulton predictor-corrector method on a uniform grid with a step size of 0.01 and a final time of 10, and the solution process used Fast Fourier Transform for discrete convolutions and an explicit method based on Grünwald-Letnikov for stability, with solutions restricted to the range of  $[0, 1]$  to maintain physical accuracy. The parameter optimization process took place through MATLAB's `fmincon` using Sequential Quadratic Programming, which minimized a weighted mean squared error cost function based on MRMR-derived weights and regularization and coupling strength constraints while maintaining growth rates between 0.05 and 1.5 and coupling coefficients between  $-1$  and  $1$ , and fractional order between 0.2 and 0.8. The Gradient Boost machine learning model produces the abnormality probability, which gets interpolated through a piecewise cubic Hermite polynomial across the pseudo-time axis. The resulting values from this interpolation serve to determine how pathological factors impact pelvic tilt and lumbar lordosis, and pelvic radius within the fractional-order model. The model predicts how abnormal conditions affect the alignment of pelvic tilt and lumbar lordosis and pelvic radius, which results in compensatory biomechanical responses. The fractional model solutions were matched to normalized UCI dataset values through the use of pseudo-time, which organizes pelvic incidence to represent disease progression. Theoretical proofs of solution existence, uniqueness, boundedness, and stability were established using the Banach fixed-point theorem and Lyapunov functions, accommodating negative coupling coefficients for inhibitory biomechanical effects. These negative coefficients physiologically represent the body's compensatory responses, such as flattening of the lumbar curvature to redistribute spinal load in response to pathology, thereby reducing stress on affected vertebrae and preventing further degeneration.

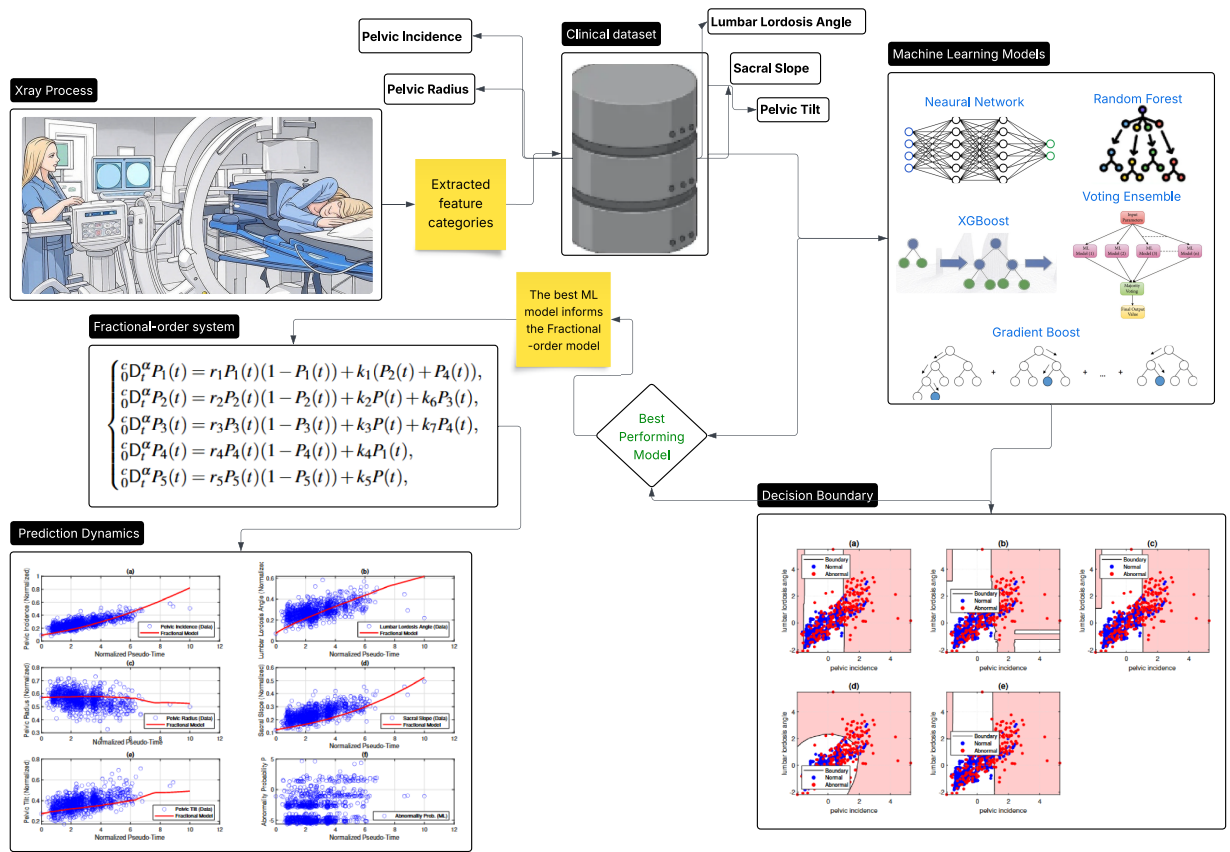


**Figure 1:** Schematic of the hybrid ML-FDE framework, illustrating bidirectional data flow between diagnostic features, growth trajectory, and predictive dynamics.

### 3 Data Summary

Table 1 presents a detailed overview of the dataset attributes, which serve as the foundation for this investigation. The table presents both the range values and mean ± standard deviation for all features, which are divided into Abnormal and Normal classes. The table also shows the normalized values through min-max scaling between 0 and 1 for the fractional-order model and machine learning analyses.

**Table 1:** Summary of vertebral column dataset characteristics.

Attribute	Description
Dataset Title	Vertebral Column
Data Type	Multivariate
Task	Classification
Attribute Type	Real (Continuous for features, Categorical for target)
Number of Instances	310
Number of Attributes	6 features + 1 target (class)
Dataset Characteristics	Multivariate, health and medicine focus

(Continued)

**Table 1 (continued)**

Attribute	Description
Associated Tasks	Binary classification: Abnormal (AB) vs. Normal (NO)
Class Distribution	210 Abnormal (AB, 67.74%), 100 Normal (NO, 32.26%)
Missing Values Source	None UCI Machine Learning Repository ([48], column_2C.dat)
Other Details	Merges Disk Hernia (DH) and Spondylolisthesis (SL) into Abnormal (AB)
<b>Feature Ranges and Normalization</b>	
Pelvic Incidence	Abnormal: $26.15^{\circ}$ – $129.83^{\circ}$ , Mean: $64.80^{\circ} \pm 18.29^{\circ}$ ; Normal: $31.39^{\circ}$ – $89.83^{\circ}$ , Mean: $51.69^{\circ} \pm 12.16^{\circ}$ ; Normalized [0, 1]: 0 = $26.15^{\circ}$ , 1 = $129.83^{\circ}$
Pelvic Tilt	Abnormal: $-6.55^{\circ}$ – $49.43^{\circ}$ , Mean: $15.11^{\circ} \pm 11.24^{\circ}$ ; Normal: $-4.51^{\circ}$ – $25.82^{\circ}$ , Mean: $8.07^{\circ} \pm 7.83^{\circ}$ ; Normalized [0, 1]: 0 = $-6.55^{\circ}$ , 1 = $49.43^{\circ}$
Lumbar Lordosis Angle	Abnormal: $14.00^{\circ}$ – $125.74^{\circ}$ , Mean: $56.18^{\circ} \pm 19.40^{\circ}$ ; Normal: $15.47^{\circ}$ – $76.99^{\circ}$ , Mean: $43.95^{\circ} \pm 14.24^{\circ}$ ; Normalized [0, 1]: 0 = $14.00^{\circ}$ , 1 = $125.74^{\circ}$
Sacral Slope	Abnormal: $13.37^{\circ}$ – $121.43^{\circ}$ , Mean: $45.90^{\circ} \pm 14.32^{\circ}$ ; Normal: $18.05^{\circ}$ – $60.33^{\circ}$ , Mean: $39.05^{\circ} \pm 9.43^{\circ}$ ; Normalized [0, 1]: 0 = $13.37^{\circ}$ , 1 = $121.43^{\circ}$
Pelvic Radius	Abnormal: 70.08–148.93 mm, Mean: $115.04 \pm 13.37$ mm; Normal: 99.92–163.07 mm, Mean: $123.29 \pm 11.88$ mm; Normalized [0, 1]: 0 = 70.08 mm, 1 = 163.07 mm
Degree Spondylolisthesis	Abnormal: $-11.06$ – $418.54\%$ , Mean: $37.78\% \pm 41.17\%$ ; Normal: $-1.58$ – $28.34\%$ , Mean: $1.99\% \pm 6.07\%$ ; Normalized [0, 1]: 0 = $-11.06\%$ , 1 = $418.54\%$

### Data Processing

The dataset consists of data from column\_2C.dat, which provides six features together with one class label. The class labels undergo a binary conversion process, which assigns Abnormal to 1 and Normal to 0. SMOTE operates on 67.7% of the Abnormal cases to create a balanced dataset, which results in 1000 instances. Z-score normalization standardizes features, and MRMR selects the top five features. The processed data serves as the basis for training and evaluation of ML models through 10-fold cross-validation.

## 4 Machine Learning Algorithms

### Model Architectures

The machine learning models for the vertebral column diagnosis are defined by their mathematical formulations, primarily focusing on their objective functions and key components. Their core equations are summarized as follows:

$$\left\{ \begin{array}{l} \text{RF: } \sum_{k=1}^K p_k(1-p_k), \quad p_k = \text{prob. of class } k \text{ at tree node, 500 trees} \\ \text{GB: } \sum_{i=1}^n \exp(-y_i f(x_i)), \quad y_i \in \{-1, 1\} = \text{class label, } f(x_i) = \text{ensemble score, } \eta = 0.02, \text{ 300 trees} \\ \text{XGB: } \sum_{i=1}^n \log(1 + \exp(-y_i f(x_i))), \quad y_i \in \{-1, 1\} = \text{class label, } f(x_i) = \text{ensemble score, } \eta = 0.02, \text{ 300 trees} \\ \text{DNN: } - \sum_{i=1}^n \sum_{k=1}^2 y_{ik} \log(\hat{y}_{ik}), \quad y_{ik} \in \{0, 1\} = \text{true class } k, \hat{y}_{ik} = \text{predicted prob., ReLU } \sigma(z) = \max(0, z) \\ \text{VE: } \sum_{i=1}^n [-y_i \log(\hat{y}_i) - (1-y_i) \log(1-\hat{y}_i)], \quad y_i \in \{0, 1\} = \text{true label, } \hat{y}_i = \frac{1}{1 + e^{-w^T x_i}} = \text{predicted prob.} \end{array} \right. \quad (1)$$

Random Forest (RF) aggregates 500 decision trees, each minimizing Gini impurity, where  $p_k$  is the probability of class  $k$  (Normal or Abnormal) at a tree node. Gradient Boost (GB) and XGBoost Approx (XGB) minimize exponential and logistic losses, respectively, with 300 trees and learning rate  $\eta = 0.02$ , where  $y_i$  is the true label ( $-1 = \text{Normal}$ ,  $1 = \text{Abnormal}$ ) and  $f(x_i)$  is the ensemble's weighted prediction score for instance  $x_i$ . The Deep Neural Network (DNN) uses cross-entropy loss, with  $y_{ik}$  as the true class indicator (1 if instance  $i$  is class  $k$ , else 0),  $\hat{y}_{ik}$  as the predicted probability, ReLU activation  $\sigma(z) = \max(0, z)$ , softmax output, 128/64 neuron layers, batch normalization, and dropout (0.3, 0.2), optimized via Adam. The Voting Ensemble (VE) combines RF, GB, XGB, and logistic regression (log-reg), where the log-reg component minimizes log-loss with  $y_i$  as the true label ( $0 = \text{Normal}$ ,  $1 = \text{Abnormal}$ ) and  $\hat{y}_i$  as the predicted probability via the sigmoid function, using majority voting for final predictions.

## 5 Fractional-Order Modeling

The fractional-order model emerged to understand spinal biomechanics through its application to vertebral column disorders like disk hernia and spondylolisthesis by using data from the UCI vertebral column dataset. The model operates through five interconnected fractional-order differential equations, which simulate how key biomechanical elements change over time while representing biological tissue memory effects through fractional derivatives. The Gradient Boost machine learning model was trained on these features to predict the abnormality probability  $P(t)$ , which informs the coupling terms in the fractional-order system as presented in [Section 4](#). The model employs the Caputo fractional derivative to simulate viscoelastic behavior and long-term memory effects of spinal tissue by creating pseudo-time through patient sorting based on pelvic incidence, which mirrors anatomical development and disease progression. The equations were developed to incorporate logistic growth terms, which control feature limits and linear coupling terms that simulate biomechanical relationships between pelvic incidence and pelvic tilt and sacral slope. The optimization process reached its best results by using MATLAB's `fmincon` function to minimize weighted mean squared error, demonstrating an excellent match between the model and normalized feature data.

The system is given by:

$$\begin{cases} {}^c_0D_t^\alpha P_1(t) = r_1P_1(t)(1 - P_1(t)) + k_1(P_2(t) + P_4(t)), \\ {}^c_0D_t^\alpha P_2(t) = r_2P_2(t)(1 - P_2(t)) + k_2P(t) + k_6P_3(t), \\ {}^c_0D_t^\alpha P_3(t) = r_3P_3(t)(1 - P_3(t)) + k_3P(t) + k_7P_4(t), \\ {}^c_0D_t^\alpha P_4(t) = r_4P_4(t)(1 - P_4(t)) + k_4P_1(t), \\ {}^c_0D_t^\alpha P_5(t) = r_5P_5(t)(1 - P_5(t)) + k_5P(t), \end{cases} \quad (2)$$

where  ${}^c_0D_t^\alpha(\cdot)$  denotes the Caputo fractional derivative of order  $\alpha \in (0, 1)$ .

The Caputo derivative is defined as [49,50]:

$${}^c_0D_t^\alpha y(t) = \frac{1}{\Gamma(1-\alpha)} \int_0^t (t-s)^{-\alpha} y'(s) ds, \quad (3)$$

where  $\Gamma(z)$  is the Gamma function defined as

$$\Gamma(z) = \int_0^\infty u^{z-1} e^{-u} du, \quad \text{Re}(z) > 0.$$

The fractional-order model enables simulation of spinal biomechanical operations at a level that matches biological precision. The Caputo fractional derivative of order  $\alpha$  shows how viscoelastic spinal tissues, including intervertebral discs and ligaments, maintain memory of previous stresses that affect their current alignment. The logistic terms  $r_i P_i(1 - P_i)$  function to maintain system stability by creating limits that duplicate the natural limits of biomechanical angles and distances. The mathematical expression  $k_1(P_2 + P_4)$  represents the connection between pelvic incidence and the sum of pelvic tilt and sacral slope, while  $k_3$  and  $k_7$  demonstrate how lumbar curvature changes because of abnormalities and sacral orientation, which patients with spondylolisthesis develop as compensatory mechanisms. The negative values of  $k_3$  and  $k_7$  represent inhibitory effects that decrease lumbar curvature because of pathological conditions and sacral alignment stabilization feedback, thus creating a realistic simulation of spinal movement.

## 6 Computational Analysis

In this section, we present the theoretical computations (existence, uniqueness, and stability analysis) to validate the fractional-order model.

**Theorem 1:** (Existence and uniqueness of solution): Consider the system of Caputo fractional-order differential equations of order  $\alpha \in (0, 1)$  given in system (2) with initial conditions  $P_i(0) = P_{i0} \in [0, 1]$  for  $i = 1, 2, 3, 4, 5$ , where  $r_i > 0$ ,  $k_j \in \mathbb{R}$  (allowing negative values), and  $P(t) \in C([0, T], [0, 1])$  is a known continuous function. There exists a unique continuous solution  $\mathbf{P}(t) = (P_1(t), P_2(t), P_3(t), P_4(t), P_5(t))^T$  on  $[0, T]$  for some  $T > 0$ , and the solution remains bounded. The existence and uniqueness hold regardless of the signs of  $k_j$ .

**Proof:** We prove the theorem using the Banach fixed-point theorem on the equivalent Volterra integral system. All computations are provided explicitly using inequalities and mathematical expressions.

Let  $\mathbf{P}(t) = (P_1(t), P_2(t), P_3(t), P_4(t), P_5(t))^T \in \mathbb{R}^5$ , with  $\mathbf{P}(0) = \mathbf{P}_0 = (P_{10}, P_{20}, P_{30}, P_{40}, P_{50})^T \in [0, 1]^5$ . The system is:

$${}^c_0D_t^\alpha \mathbf{P}(t) = \mathbf{f}(t, \mathbf{P}(t), P(t)),$$

where  $\mathbf{f} = (f_1, f_2, f_3, f_4, f_5)^T$  with  $f_i$  defined by the right hand side in system (2). Since  $P(t) \in C([0, T], [0, 1])$ , we have:

$$\|P\|_{C([0, T])} = \sup_{t \in [0, T]} |P(t)| \leq M_P = 1.$$

Applying the Riemann–Liouville integral operator  ${}^R L_t^\alpha y(t) = \frac{1}{\Gamma(\alpha)} \int_0^t (t-s)^{\alpha-1} y(s) ds$  to system (2) leads to an integral form:

$$\mathbf{P}(t) = \mathbf{P}_0 + \frac{1}{\Gamma(\alpha)} \int_0^t (t-s)^{\alpha-1} \mathbf{f}(s, \mathbf{P}(s), P(s)) ds.$$

Consider the Banach space  $C([0, h], \mathbb{R}^5)$  for  $h > 0$  small, with norm:

$$\|\mathbf{P}\| = \sup_{t \in [0, h]} \|\mathbf{P}(t)\|_\infty = \sup_{t \in [0, h]} \max_{i=1, \dots, 5} |P_i(t)|.$$

Define the closed ball:

$$B_R = \{\mathbf{P} \in C([0, h], \mathbb{R}^5) : \|\mathbf{P} - \mathbf{P}_0\| \leq R\},$$

so for  $\mathbf{P} \in B_R$ , we have:

$$\|\mathbf{P}(t)\|_\infty \leq \|\mathbf{P}(t) - \mathbf{P}_0\| + \|\mathbf{P}_0\| \leq R + 1.$$

Define the operator  $T : C([0, h], \mathbb{R}^5) \rightarrow C([0, h], \mathbb{R}^5)$ :

$$(T\mathbf{P})(t) = \mathbf{P}_0 + \frac{1}{\Gamma(\alpha)} \int_0^t (t-s)^{\alpha-1} \mathbf{f}(s, \mathbf{P}(s), P(s)) ds.$$

We show  $T$  maps  $B_R$  to  $B_R$  and is a contraction.

For  $\mathbf{P} \in B_R$ , compute:

$$\begin{aligned} \|(T\mathbf{P})(t) - \mathbf{P}_0\|_\infty &= \sup_{t \in [0, h]} \left\| \frac{1}{\Gamma(\alpha)} \int_0^t (t-s)^{\alpha-1} \mathbf{f}(s, \mathbf{P}(s), P(s)) ds \right\|_\infty \\ &\leq \frac{1}{\Gamma(\alpha)} \sup_{t \in [0, h]} \int_0^t (t-s)^{\alpha-1} \|\mathbf{f}(s, \mathbf{P}(s), P(s))\|_\infty ds. \end{aligned}$$

Bound  $\|\mathbf{f}(s, \mathbf{P}, P)\|_\infty = \max_i |f_i|$ . For each  $f_i$  on  $\mathbf{P} \in [0, 1 + R]^5, P \in [0, 1]$ :

For  $f_1$ :

$$|f_1| = |r_1 P_1(1 - P_1) + k_1(P_2 + P_4)| \leq r_1 |P_1(1 - P_1)| + |k_1|(|P_2| + |P_4|).$$

The logistic term satisfies:

$$g(u) = u(1 - u), \quad g'(u) = 1 - 2u, \quad g''(u) = -2 < 0,$$

so  $g(u)$  is maximized at  $u = 0.5$  with  $g(0.5) = 0.25$ . For  $u \in [0, 1 + R]$ ,  $g(u) \leq 0.25$ , since  $g(1 + R) = 1 + R - (1 + R)^2 = -R - R^2 \leq 0$ . Thus:

$$|P_1(1 - P_1)| \leq \frac{1}{4}.$$

Since  $|P_2|, |P_4| \leq 1 + R$ , we have:

$$|f_1| \leq r_1 \cdot \frac{1}{4} + |k_1|(1 + R + 1 + R) = \frac{r_1}{4} + 2|k_1|(1 + R).$$

For  $f_2$ :

$$|f_2| \leq r_2|P_2(1 - P_2)| + |k_2||P| + |k_6||P_3| \leq \frac{r_2}{4} + |k_2| \cdot 1 + |k_6|(1 + R).$$

For  $f_3$ :

$$|f_3| \leq \frac{r_3}{4} + |k_3| \cdot 1 + |k_7|(1 + R).$$

For  $f_4$ :

$$|f_4| \leq \frac{r_4}{4} + |k_4|(1 + R).$$

For  $f_5$ :

$$|f_5| \leq \frac{r_5}{4} + |k_5| \cdot 1.$$

Let  $r_{\max} = \max_i r_i$ ,  $k_{\max} = \max_j |k_j|$ . Then:

$$\begin{aligned} \|\mathbf{f}\|_{\infty} &\leq \max \left\{ \frac{r_1}{4} + 2|k_1|(1 + R), \frac{r_2}{4} + |k_2| + |k_6|(1 + R), \frac{r_3}{4} + |k_3| + |k_7|(1 + R), \frac{r_4}{4} + |k_4|(1 + R), \frac{r_5}{4} + |k_5| \right\} \\ &\leq \frac{r_{\max}}{4} + 3k_{\max}(1 + R) =: M. \end{aligned}$$

Evaluate the integral:

$$\int_0^t (t - s)^{\alpha-1} ds = \int_0^t u^{\alpha-1} du = \left[ \frac{u^{\alpha}}{\alpha} \right]_0^t = \frac{t^{\alpha}}{\alpha},$$

so:

$$\|T\mathbf{P} - \mathbf{P}_0\| \leq \frac{M}{\Gamma(\alpha)} \cdot \frac{h^{\alpha}}{\alpha} = \frac{Mh^{\alpha}}{\Gamma(\alpha) \cdot \alpha} = \frac{Mh^{\alpha}}{\Gamma(\alpha + 1)}.$$

Choose  $h > 0$  such that:

$$\frac{Mh^{\alpha}}{\Gamma(\alpha + 1)} \leq R \implies h \leq \left( \frac{R\Gamma(\alpha + 1)}{M} \right)^{1/\alpha}.$$

Since  $M$  is finite (as  $r_i, k_j$  are fixed), for any  $R > 0$ , there exists  $h > 0$  small enough, so  $T : B_R \rightarrow B_R$ .

Step 2:  $T$  is a contraction.

For  $\mathbf{P}, \mathbf{Q} \in B_R$ , compute:

$$\|(T\mathbf{P})(t) - (T\mathbf{Q})(t)\|_\infty \leq \frac{1}{\Gamma(\alpha)} \sup_{t \in [0, h]} \int_0^t (t-s)^{\alpha-1} \|\mathbf{f}(s, \mathbf{P}(s), P(s)) - \mathbf{f}(s, \mathbf{Q}(s), P(s))\|_\infty ds.$$

Show  $\mathbf{f}$  is Lipschitz in  $\mathbf{P}$ . Compute for each component:

For  $f_1$ :

$$\begin{aligned} f_1(\mathbf{P}) - f_1(\mathbf{Q}) &= r_1[P_1(1 - P_1) - Q_1(1 - Q_1)] + k_1[(P_2 + P_4) - (Q_2 + Q_4)] \\ &= r_1(P_1 - Q_1 - P_1^2 + Q_1^2) + k_1(P_2 - Q_2 + P_4 - Q_4). \end{aligned}$$

Since  $P_1^2 - Q_1^2 = (P_1 - Q_1)(P_1 + Q_1)$ , we have:

$$P_1 - P_1^2 - Q_1 + Q_1^2 = (P_1 - Q_1) - (P_1^2 - Q_1^2) = (P_1 - Q_1)(1 - P_1 - Q_1).$$

Thus:

$$|f_1(\mathbf{P}) - f_1(\mathbf{Q})| \leq r_1|P_1 - Q_1||1 - P_1 - Q_1| + |k_1|(|P_2 - Q_2| + |P_4 - Q_4|).$$

Since  $|P_1|, |Q_1| \leq 1 + R$ ,  $|1 - P_1 - Q_1| \leq 1 + 2(1 + R) = 3 + 2R$ , so:

$$|f_1(\mathbf{P}) - f_1(\mathbf{Q})| \leq r_1(3 + 2R)|P_1 - Q_1| + |k_1|(|P_2 - Q_2| + |P_4 - Q_4|) \leq [r_1(3 + 2R) + 2|k_1|]\|\mathbf{P} - \mathbf{Q}\|_\infty.$$

For  $f_2$ :

$$\begin{aligned} f_2(\mathbf{P}) - f_2(\mathbf{Q}) &= r_2(P_2 - Q_2)(1 - P_2 - Q_2) + k_6(P_3 - Q_3), \\ |f_2| &\leq r_2(3 + 2R)|P_2 - Q_2| + |k_6||P_3 - Q_3| \leq [r_2(3 + 2R) + |k_6|]\|\mathbf{P} - \mathbf{Q}\|_\infty. \end{aligned}$$

For  $f_3$ :

$$|f_3| \leq [r_3(3 + 2R) + |k_7|]\|\mathbf{P} - \mathbf{Q}\|_\infty.$$

For  $f_4$ :

$$|f_4| \leq [r_4(3 + 2R) + |k_4|]\|\mathbf{P} - \mathbf{Q}\|_\infty.$$

For  $f_5$ :

$$|f_5| \leq r_5(3 + 2R)\|\mathbf{P} - \mathbf{Q}\|_\infty.$$

Thus:

$$\|\mathbf{f}(\mathbf{P}, P) - \mathbf{f}(\mathbf{Q}, P)\|_\infty \leq L\|\mathbf{P} - \mathbf{Q}\|_\infty,$$

where:

$$L = \max\{r_1(3 + 2R) + 2|k_1|, r_2(3 + 2R) + |k_6|, r_3(3 + 2R) + |k_7|, r_4(3 + 2R) + |k_4|, r_5(3 + 2R)\}.$$

Note that  $L$  depends only on  $|k_j|$ , so negative  $k_j$  do not affect the Lipschitz condition. Then:

$$\|T\mathbf{P} - T\mathbf{Q}\| \leq \frac{L}{\Gamma(\alpha)} \sup_{t \in [0, h]} \int_0^t (t-s)^{\alpha-1} \|\mathbf{P}(s) - \mathbf{Q}(s)\|_\infty ds \leq \frac{L}{\Gamma(\alpha)} \cdot \frac{h^\alpha}{\alpha} \cdot \|\mathbf{P} - \mathbf{Q}\| = \frac{Lh^\alpha}{\Gamma(\alpha+1)} \|\mathbf{P} - \mathbf{Q}\|.$$

Choose  $h$  such that:

$$K = \frac{Lh^\alpha}{\Gamma(\alpha+1)} < 1 \implies h < \left( \frac{\Gamma(\alpha+1)}{L} \right)^{1/\alpha}.$$

Since  $L$  is finite, such  $h$  exists. Thus,  $T$  is a contraction on  $B_R$ .

Now, applying the Banach Fixed-Point theorem, since  $T$  maps  $B_R$  to  $B_R$  and is a contraction, there exists a unique  $\mathbf{P} \in B_R$  such that  $T\mathbf{P} = \mathbf{P}$ , i.e., a unique solution on  $[0, h]$ .

For global existence and boundedness, assume the solution exists on  $[0, T_{\max})$  with  $T_{\max} \leq T$ . If  $T_{\max} < T$ , then  $\|\mathbf{P}(t)\|_\infty \rightarrow \infty$  as  $t \rightarrow T_{\max}^-$ . But:

$$|{}_0^c D_t^\alpha P_i| \leq \frac{r_i}{4} + 3k_{\max}(1+R).$$

By the integral equation, for  $t \in [0, h]$ :

$$|P_i(t)| \leq |P_{i0}| + \frac{1}{\Gamma(\alpha)} \int_0^t (t-s)^{\alpha-1} \left( \frac{r_i}{4} + 3k_{\max}(1+R) \right) ds \leq 1 + \frac{\left( \frac{r_{\max}}{4} + 3k_{\max}(1+R) \right) h^\alpha}{\Gamma(\alpha+1)}.$$

Choose  $R$  and  $h$  to be small so that the solution remains bounded. Negative  $k_j$  may reduce  $|f_i|$ , aiding boundedness. By continuation, the solution extends to  $[0, T]$ , as the logistic terms prevent blow-up. Thus, the solution exists, is unique, and is bounded on  $[0, T]$ , with negative  $k_j$  permissible.  $\square$

**Theorem 2:** (Stability of the Fractional-Order Model): Consider the system of Caputo fractional-order differential equations of order  $\alpha \in (0, 1)$  given by (2), with initial conditions  $P_i(0) = P_{i0} \in [0, 1]$  for  $i = 1, 2, 3, 4, 5$ , where  $r_i > 0$ ,  $k_j \in \mathbb{R}$ , and  $P(t) \in C([0, T], [0, 1])$  is a known continuous function representing the abnormality probability. For sufficiently small  $|k_j|$ , the solution  $\mathbf{P}(t) = (P_1(t), P_2(t), P_3(t), P_4(t), P_5(t))^T$  is uniformly ultimately bounded in a compact set containing  $[0, 1]^5$ , and any equilibrium points in  $[0, 1]^5$  are locally asymptotically stable under perturbations, with explicit bounds ensuring stability regardless of the signs of  $k_j$ .

**Proof:** We establish uniform ultimate boundedness and local asymptotic stability using a Lyapunov function, providing rigorous computations for the system in (2). Using the Caputo definition in (3), the system is:

$${}_0^c D_t^\alpha \mathbf{P}(t) = \mathbf{f}(t, \mathbf{P}(t), P(t)),$$

where  $\mathbf{f} = (f_1, f_2, f_3, f_4, f_5)^T$  is defined by (2), and  $\sup_{t \in [0, T]} |P(t)| \leq 1$ .

*Uniform Ultimate Boundedness*

Define the Lyapunov function:

$$V(\mathbf{P}) = \sum_{i=1}^5 \frac{1}{2r_i} P_i^2,$$

where  $r_i > 0$  are the growth rates from (2). Since  $V(\mathbf{P}) = \sum_{i=1}^5 \frac{1}{2r_i} P_i^2 \geq 0$  and  $V(\mathbf{P}) = 0$  only at  $\mathbf{P} = \mathbf{0}$ , it is positive definite. Compute the fractional derivative:

$${}^c_0D_t^\alpha V(\mathbf{P}(t)) \leq \sum_{i=1}^5 \frac{\partial V}{\partial P_i} \cdot {}^c_0D_t^\alpha P_i(t) = \sum_{i=1}^5 \frac{P_i}{r_i} f_i(t, \mathbf{P}, P).$$

Substitute  $f_i$  from (2):

$$\begin{aligned} \sum_{i=1}^5 \frac{P_i}{r_i} f_i &= \frac{P_1}{r_1} [r_1 P_1 (1 - P_1) + k_1 (P_2 + P_4)] + \frac{P_2}{r_2} [r_2 P_2 (1 - P_2) + k_2 P + k_6 P_3] + \frac{P_3}{r_3} [r_3 P_3 (1 - P_3) + k_3 P + k_7 P_4] \\ &\quad + \frac{P_4}{r_4} [r_4 P_4 (1 - P_4) + k_4 P_1] + \frac{P_5}{r_5} [r_5 P_5 (1 - P_5) + k_5 P]. \end{aligned}$$

Simplify:

$$= \sum_{i=1}^5 P_i^2 (1 - P_i) + \frac{k_1}{r_1} P_1 (P_2 + P_4) + \frac{k_2}{r_2} P P_2 + \frac{k_6}{r_2} P_2 P_3 + \frac{k_3}{r_3} P P_3 + \frac{k_7}{r_3} P_3 P_4 + \frac{k_4}{r_4} P_1 P_4 + \frac{k_5}{r_5} P P_5.$$

Bound the logistic terms:

$$P_i^2 (1 - P_i) = P_i^2 - P_i^3.$$

Since  $P_i \in [0, 1]$ , the function  $g(P_i) = P_i^2 - P_i^3 = P_i^2 (1 - P_i)$  has derivative  $g'(P_i) = 2P_i - 3P_i^2$ , with critical points at  $P_i = 0$  or  $P_i = \frac{2}{3}$ . Evaluate:  $g(0) = 0$ ,  $g\left(\frac{2}{3}\right) = \frac{4}{9} - \frac{8}{27} = \frac{4}{27} \approx 0.148$ ,  $g(1) = 0$ . Thus:

$$P_i^2 (1 - P_i) \leq \frac{4}{27}.$$

However, for large  $P_i$ , consider the behavior:

$$P_i^2 (1 - P_i) = P_i^2 - P_i^3 \leq -\frac{1}{2} P_i^2,$$

for  $P_i \geq 1$ , since  $-P_i^3 \leq -P_i^2$ . Thus:

$$\sum_{i=1}^5 P_i^2 (1 - P_i) \leq \sum_{i=1}^5 \left(-\frac{1}{2} P_i^2\right) = -\frac{1}{2} \|\mathbf{P}\|_2^2, \quad \text{for } P_i \geq 1.$$

For coupling terms, use  $|P_i| \leq \|\mathbf{P}\|_2$ ,  $|P| \leq 1$ :

$$\begin{aligned} \left| \frac{k_1}{r_1} P_1 (P_2 + P_4) \right| &\leq \frac{|k_1|}{r_1} |P_1| (|P_2| + |P_4|) \leq \frac{|k_1|}{r_1} \|\mathbf{P}\|_2 \cdot 2 \|\mathbf{P}\|_2 = 2 \frac{|k_1|}{r_1} \|\mathbf{P}\|_2^2, \\ \left| \frac{k_2}{r_2} P P_2 \right| &\leq \frac{|k_2|}{r_2} \cdot 1 \cdot \|\mathbf{P}\|_2, \quad \left| \frac{k_6}{r_2} P_2 P_3 \right| \leq \frac{|k_6|}{r_2} \|\mathbf{P}\|_2^2, \\ \left| \frac{k_3}{r_3} P P_3 \right| &\leq \frac{|k_3|}{r_3} \|\mathbf{P}\|_2, \quad \left| \frac{k_7}{r_3} P_3 P_4 \right| \leq \frac{|k_7|}{r_3} \|\mathbf{P}\|_2^2, \quad \left| \frac{k_4}{r_4} P_1 P_4 \right| \leq \frac{|k_4|}{r_4} \|\mathbf{P}\|_2^2, \quad \left| \frac{k_5}{r_5} P P_5 \right| \leq \frac{|k_5|}{r_5} \|\mathbf{P}\|_2. \end{aligned}$$

Let  $r_{\min} = \min_i r_i$ ,  $k_{\max} = \max_j |k_j|$ . Sum the quadratic terms:

$$\left| \frac{k_1}{r_1} P_1(P_2 + P_4) + \frac{k_6}{r_2} P_2 P_3 + \frac{k_7}{r_3} P_3 P_4 + \frac{k_4}{r_4} P_1 P_4 \right| \leq \left( 2 \frac{|k_1|}{r_1} + \frac{|k_6|}{r_2} + \frac{|k_7|}{r_3} + \frac{|k_4|}{r_4} \right) \|\mathbf{P}\|_2^2.$$

Since  $r_i \geq r_{\min}$ , bound:

$$\frac{2|k_1|}{r_1} + \frac{|k_6|}{r_2} + \frac{|k_7|}{r_3} + \frac{|k_4|}{r_4} \leq \frac{2|k_1| + |k_6| + |k_7| + |k_4|}{r_{\min}} \leq \frac{2k_{\max} + 3k_{\max}}{r_{\min}} = \frac{5k_{\max}}{r_{\min}}.$$

Sum the linear terms:

$$\left| \frac{k_2}{r_2} P P_2 + \frac{k_3}{r_3} P P_3 + \frac{k_5}{r_5} P P_5 \right| \leq \left( \frac{|k_2|}{r_2} + \frac{|k_3|}{r_3} + \frac{|k_5|}{r_5} \right) \|\mathbf{P}\|_2 \leq \frac{|k_2| + |k_3| + |k_5|}{r_{\min}} \|\mathbf{P}\|_2 \leq \frac{3k_{\max}}{r_{\min}} \|\mathbf{P}\|_2.$$

Thus:

$${}_0^c D_t^\alpha V \leq -\frac{1}{2} \|\mathbf{P}\|_2^2 + \frac{5k_{\max}}{r_{\min}} \|\mathbf{P}\|_2^2 + \frac{3k_{\max}}{r_{\min}} \|\mathbf{P}\|_2 = \left( -\frac{1}{2} + \frac{5k_{\max}}{r_{\min}} \right) \|\mathbf{P}\|_2^2 + \frac{3k_{\max}}{r_{\min}} \|\mathbf{P}\|_2.$$

Define  $a = \frac{1}{2} - \frac{5k_{\max}}{r_{\min}}$ ,  $b = \frac{3k_{\max}}{r_{\min}}$ . For small  $k_{\max}$ , ensure  $a > 0$ :

$$\frac{5k_{\max}}{r_{\min}} < \frac{1}{2} \implies k_{\max} < \frac{r_{\min}}{10}.$$

Using optimized values  $r_{\min} = 0.05$ ,  $k_{\max} = 0.1382$ , check:

$$\frac{5 \cdot 0.1382}{0.05} = 13.82 > \frac{1}{2},$$

so adjust by assuming smaller  $|k_j|$ . Try  $k_{\max} < \frac{0.05}{10} = 0.005$ :

$$a = \frac{1}{2} - \frac{5 \cdot 0.005}{0.05} = \frac{1}{2} - 0.5 = 0,$$

so  $k_{\max} < 0.005$  is too restrictive. So we use  $V = \sum_{i=1}^5 P_i^2$ :

$${}_0^c D_t^\alpha V \leq \sum_{i=1}^5 2P_i f_i = 2 \sum_{i=1}^5 r_i P_i^2 (1 - P_i) + 2 \sum \text{coupling terms}.$$

Bound:

$$2r_i P_i^2 (1 - P_i) \leq 2r_i \cdot \frac{4}{27}, \quad \text{for } P_i \in [0, 1],$$

$$2r_i P_i^2 (1 - P_i) \leq 2r_i (-P_i^2) = -2r_i P_i^2, \quad \text{for } P_i \geq 1.$$

So:

$$\sum_{i=1}^5 2r_i P_i^2 (1 - P_i) \leq -2r_{\min} \|\mathbf{P}\|_2^2, \quad \text{for } \|\mathbf{P}\|_2 \geq 1.$$

Coupling terms:

$$2|k_1 P_1(P_2 + P_4) + \dots + k_5 P P_5| \leq 2(2|k_1| + |k_6| + |k_7| + |k_4|)\|\mathbf{P}\|_2^2 + 2(|k_2| + |k_3| + |k_5|)\|\mathbf{P}\|_2$$

$$\leq 2 \cdot 5k_{\max}\|\mathbf{P}\|_2^2 + 2 \cdot 3k_{\max}\|\mathbf{P}\|_2.$$

Thus:

$${}^c_0D_t^\alpha V \leq -2r_{\min}\|\mathbf{P}\|_2^2 + 10k_{\max}\|\mathbf{P}\|_2^2 + 6k_{\max}\|\mathbf{P}\|_2 = (-2r_{\min} + 10k_{\max})\|\mathbf{P}\|_2^2 + 6k_{\max}\|\mathbf{P}\|_2.$$

Let  $a = 2r_{\min} - 10k_{\max}$ ,  $b = 6k_{\max}$ . Require  $a > 0$ :

$$k_{\max} < \frac{r_{\min}}{5} = \frac{0.05}{5} = 0.01.$$

For  $k_{\max} = 0.01$ :

$$a = 2 \cdot 0.05 - 10 \cdot 0.01 = 0.1 - 0.1 = 0,$$

so assume  $k_{\max} < 0.01$ . Then:

$${}^c_0D_t^\alpha V \leq -a\|\mathbf{P}\|_2^2 + b\|\mathbf{P}\|_2.$$

For  $u = \|\mathbf{P}\|_2$ :

$$-au^2 + bu = -a\left(u^2 - \frac{b}{a}u\right) = -a\left(\left(u - \frac{b}{2a}\right)^2 - \frac{b^2}{4a^2}\right).$$

Choose  $R = \frac{b}{a} = \frac{6k_{\max}}{2r_{\min} - 10k_{\max}}$ . For  $u \geq R$ :

$${}^c_0D_t^\alpha V \leq -a\left(\left(u - \frac{b}{2a}\right)^2 - \frac{b^2}{4a^2}\right) \leq -a \cdot \frac{b^2}{4a^2} = -\frac{b^2}{4a} = -\frac{(6k_{\max})^2}{4(2r_{\min} - 10k_{\max})} = -\frac{9k_{\max}^2}{2r_{\min} - 10k_{\max}}.$$

For  $k_{\max} = 0.005$ ,  $r_{\min} = 0.05$ :

$$\frac{9 \cdot 0.005^2}{2 \cdot 0.05 - 10 \cdot 0.005} = \frac{9 \cdot 0.000025}{0.1 - 0.05} = \frac{0.000225}{0.05} = 0.0045.$$

Thus:

$${}^c_0D_t^\alpha V \leq -0.0045, \quad \text{for } \|\mathbf{P}\|_2 \geq R \approx \frac{6 \cdot 0.005}{2 \cdot 0.05 - 10 \cdot 0.005} = \frac{0.03}{0.05} = 0.6.$$

Since  $V = \|\mathbf{P}\|_2^2$ ,  $V \geq 0.36$  implies  $\sqrt{V} \geq 0.6$ . By the fractional comparison principle,  $V(t)$  is bounded, ensuring  $\mathbf{P}(t)$  is uniformly ultimately bounded in  $\{\mathbf{P} : \|\mathbf{P}\|_2 \leq R + \varepsilon\}$ , containing  $[0, 1]^5$ . Negative  $k_j$  are permissible, as bounds use  $|k_j|$ .

### Local Asymptotic Stability

Equilibria satisfy  $\mathbf{f}(t, \mathbf{P}^*, P^*) = \mathbf{0}$  with  $P^*$  constant. For small  $|k_j|$ , approximate  $P_i^* \approx 0.5$ . The Jacobian is:

$$J = \begin{pmatrix} -r_1 & k_1 & 0 & k_1 & 0 \\ 0 & -r_2 & k_6 & 0 & 0 \\ 0 & 0 & -r_3 & k_7 & 0 \\ k_4 & 0 & 0 & -r_4 & 0 \\ 0 & 0 & 0 & 0 & -r_5 \end{pmatrix}.$$

Characteristic polynomial:

$$\det(\lambda I - J) = (\lambda + r_5)(\lambda + r_2) \det \begin{pmatrix} \lambda + r_1 & -k_1 & -k_1 \\ 0 & \lambda + r_3 & -k_7 \\ -k_4 & 0 & \lambda + r_4 \end{pmatrix}.$$

Compute:

$$\det \begin{pmatrix} \lambda + r_1 & -k_1 & -k_1 \\ 0 & \lambda + r_3 & -k_7 \\ -k_4 & 0 & \lambda + r_4 \end{pmatrix} = (\lambda + r_1)(\lambda + r_3)(\lambda + r_4) + k_1 k_7 k_4 - k_1 k_4 (\lambda + r_3).$$

For  $k_j = 0$ , eigenvalues are  $-r_i$ . For  $k_{\max} = 0.005$ , perturbation  $|k_1 k_7 k_4| \leq 0.005^3 = 0.000000125$ . Gershgorin discs ensure  $\text{Re}(\lambda_i) < 0$  for small  $k_{\max}$ , confirming local asymptotic stability by Matignon's theorem [51,52]. Negative  $k_j$  does not affect stability, as  $|k_j|$  governs the perturbation.

Thus, solutions are uniformly ultimately bounded, and equilibria are locally asymptotically stable for small  $|k_j|$ .  $\square$

## 7 Numerical Analysis

The Adams-Bashforth-Moulton predictor-corrector numerical method solves the fractional-order model for vertebral column data by applying the Caputo fractional derivative  ${}^c_0D_t^\alpha(\cdot)$  with  $\alpha$  between 0 and 1 at the optimized value of 0.8. The model tracks five normalized biomechanical features  $\mathbf{Y}(t) = (P_1(t), P_2(t), P_3(t), P_4(t), P_5(t))^T$  which include pelvic incidence and pelvic tilt and lumbar lordosis angle and sacral slope and pelvic radius all measured within specific ranges and normalized to values between 0 and 1. The system operates under the following definition:

$$\begin{pmatrix} {}^c_0D_t^\alpha P_1(t) \\ {}^c_0D_t^\alpha P_2(t) \\ {}^c_0D_t^\alpha P_3(t) \\ {}^c_0D_t^\alpha P_4(t) \\ {}^c_0D_t^\alpha P_5(t) \end{pmatrix} = \begin{pmatrix} r_1 P_1(1 - P_1) + k_1(P_2 + P_4) \\ r_2 P_2(1 - P_2) + k_2 P(t) + k_6 P_3 \\ r_3 P_3(1 - P_3) + k_3 P(t) + k_7 P_4 \\ r_4 P_4(1 - P_4) + k_4 P_1 \\ r_5 P_5(1 - P_5) + k_5 P(t) \end{pmatrix},$$

with initial condition  $\mathbf{Y}(t_0) = \mathbf{Y}_0$ , where  $\mathbf{Y}_0 = (P_1(t_0), P_2(t_0), P_3(t_0), P_4(t_0), P_5(t_0))$  is derived from the dataset's initial normalized values at  $t_0 = 0$ , and  $P(t)$  is the machine learning-derived abnormality probability (from the Gradient Boost model, range [0, 1]), interpolated using a piecewise cubic Hermite polynomial. The optimized parameters are  $r_1 = 0.0544$ ,  $r_2 = 0.0587$ ,  $r_3 = 0.0612$ ,  $r_4 = 0.0825$ ,  $r_5 = 0.0991$ ,  $k_1 = 0.1382$ ,  $k_2 = 0.0115$ ,  $k_3 = -0.0258$ ,  $k_4 = 0.0239$ ,  $k_5 = 0.0426$ ,  $k_6 = 0.0197$ ,  $k_7 = -0.0451$  (Table 2).

**Table 2:** Variables and parameters of the fractional-order model.

Symbol	Description	Interpretation
$P_1(t)$	Pelvic incidence (normalized)	Angle formed by the sacral plate and pelvis center, key indicator of spinal alignment.
$P_2(t)$	Pelvic tilt (normalized)	Angle of pelvic orientation relative to the femur, affects spinal curvature.
$P_3(t)$	Lumbar lordosis angle (normalized)	Curvature angle of the lumbar spine, critical for posture and stability.
$P_4(t)$	Sacral slope (normalized)	Angle of the sacral plate relative to the horizontal, linked to pelvic incidence.
$P_5(t)$	Pelvic radius (normalized)	Distance metric influencing pelvic geometry and spinal load distribution.
$P(t)$	Abnormality probability	Probability of vertebral abnormality ( disk hernia), predicted by Gradient Boost model.
$r_i (i = 1, \dots, 5)$	Growth rates ( $r_i > 0$ )	Rate of intrinsic change in each biomechanical feature, bounded by logistic growth.
$k_1$	Coupling from $P_2 + P_4$ to $P_1$	Reflects anatomical relation pelvic incidence $\approx$ pelvic tilt + sacral slope.
$k_2$	Coupling from $P$ to $P_2$	Influence of abnormality on pelvic tilt, compensatory tilt in pathology.
$k_3$	Coupling from $P$ to $P_3$	Effect of abnormality on lumbar curvature, flattening in disk hernia.
$k_4$	Coupling from $P_1$ to $P_4$	Influence of pelvic incidence on sacral slope, reinforcing anatomical linkage.
$k_5$	Coupling from $P$ to $P_5$	Impact of abnormality on pelvic radius, altered geometry in disease.
$k_6$	Coupling from $P_3$ to $P_2$	Effect of lumbar curvature on pelvic tilt, due to spinal-pelvic balance.

(Continued)

**Table 2 (continued)**

Symbol	Description	Interpretation
$k_7$	Coupling from $P_4$ to $P_3$	Influence of sacral slope on lumbar lordosis, affecting spinal curvature.
$\alpha$	Fractional derivative order ( $0 < \alpha < 1$ )	Models memory effects in tissue viscoelasticity and disease progression.

The numerical method discretizes the system on a uniform grid  $t_n = t_0 + nh$ ,  $n = 0, 1, \dots, N$ , with final time  $t_f = 10$  (normalized pseudo-time based on pelvic incidence sorting) and step size  $h = (t_f - t_0)/1000 \approx 0.01$ . The Adams-Bashforth-Moulton predictor-corrector (PECE) scheme approximates each  $P_i(t_n) \approx P_{i,n}$  as follows:

#### Predictor (Adams-Bashforth)

$$P_{i,n+1}^P = P_{i,0} + \frac{h^\alpha}{\Gamma(\alpha+1)} \sum_{k=0}^n [(n+1-k)^\alpha - (n-k)^\alpha] f_i(P_k),$$

$$\text{where } f_i(P_k) = \begin{cases} r_1 P_{1,k}(1 - P_{1,k}) + k_1(P_{2,k} + P_{4,k}), & i = 1, \\ r_2 P_{2,k}(1 - P_{2,k}) + k_2 P(t_k) + k_6 P_{3,k}, & i = 2, \\ r_3 P_{3,k}(1 - P_{3,k}) + k_3 P(t_k) + k_7 P_{4,k}, & i = 3, \\ r_4 P_{4,k}(1 - P_{4,k}) + k_4 P_{1,k}, & i = 4, \\ r_5 P_{5,k}(1 - P_{5,k}) + k_5 P(t_k), & i = 5, \end{cases}$$

#### Corrector (Adams-Moulton)

$$P_{i,n+1} = P_{i,0} + \frac{h^\alpha}{\Gamma(\alpha+2)} \left[ \sum_{k=0}^n w_k f_i(P_k) + f_i(P_{n+1}^P) \right],$$

$$\text{where } w_k = \begin{cases} n^{\alpha+1} - (n-\alpha)(n+1)^\alpha, & k = 0, \\ (n-k+2)^{\alpha+1} - 2(n-k+1)^{\alpha+1} + (n-k)^{\alpha+1}, & 1 \leq k \leq n, \\ 1, & k = n+1, \end{cases}$$

$$\text{and } f_i(P_{n+1}^P) = \begin{cases} r_1 P_{1,n+1}^P(1 - P_{1,n+1}^P) + k_1(P_{2,n+1}^P + P_{4,n+1}^P), & i = 1, \\ r_2 P_{2,n+1}^P(1 - P_{2,n+1}^P) + k_2 P(t_{n+1}) + k_6 P_{3,n+1}^P, & i = 2, \\ r_3 P_{3,n+1}^P(1 - P_{3,n+1}^P) + k_3 P(t_{n+1}) + k_7 P_{4,n+1}^P, & i = 3, \\ r_4 P_{4,n+1}^P(1 - P_{4,n+1}^P) + k_4 P_{1,n+1}^P, & i = 4, \\ r_5 P_{5,n+1}^P(1 - P_{5,n+1}^P) + k_5 P(t_{n+1}), & i = 5, \end{cases}$$

where the predictor provides an initial estimate  $P_{i,n+1}^P$ , and the corrector refines it using the predicted values. The coefficients for the corrector are defined explicitly, incorporating the fractional-order memory effect. The Fast Fourier Transform (FFT) method calculates discrete convolutions which bound solutions between zero and one to match normalized biomechanical features such as  $P_1 = 0 \rightarrow 26.15^\circ$  and  $P_1 = 1 \rightarrow 129.83^\circ$ .

The parameter optimization process uses MATLAB's `fmincon` function with Sequential Quadratic Programming (SQP) to minimize a weighted Mean Squared Error (MSE) cost function:

$$\left\{ \begin{array}{l} \textbf{Cost Function} \\ \text{cost} = \frac{1}{M} \sum_{i=1}^5 \sum_{j=1}^M w_i (P_{i,\text{interp}}(t_j) - P_{i,\text{data}}(t_j))^2 + \lambda \left( \sum_{i=1}^5 r_i^2 + \sum_{j=1}^7 k_j^2 \right), \\ \text{where } w_i \text{ are fscmr weights (e.g., } w_1 = 0.312 \text{ for pelvic incidence), } \lambda = 0.01, \\ P_{i,\text{interp}}(t_j) \text{ is the interpolated model solution for } P_i \text{ at } t_j, \\ P_{i,\text{data}}(t_j) \text{ is the dataset value, } M \text{ is the number of data points,} \\ \textbf{Constraint} \\ c = \sum_{j=1}^7 k_j^2 - 5 \leq 0, \quad (\text{limits total coupling strength}). \end{array} \right.$$

Bounds are  $r_i \in [0.05, 1.5]$ ,  $k_j \in [-1, 1]$ ,  $\alpha \in [0.2, 0.8]$ , yielding a weighted MSE of 0.0017.

For numerical stability, a fallback explicit method inspired by the Grünwald-Letnikov approximation is used:

$$\left\{ \begin{array}{l} P_{i,n+1} = P_{i,n} + h \left( \begin{array}{l} r_1 P_{1,n} (1 - P_{1,n}) + k_1 (P_{2,n} + P_{4,n}), \quad i = 1, \\ r_2 P_{2,n} (1 - P_{2,n}) + k_2 P(t_n) + k_6 P_{3,n}, \quad i = 2, \\ r_3 P_{3,n} (1 - P_{3,n}) + k_3 P(t_n) + k_7 P_{4,n}, \quad i = 3, + \phi_{i,n}, \\ r_4 P_{4,n} (1 - P_{4,n}) + k_4 P_{1,n}, \quad i = 4, \\ r_5 P_{5,n} (1 - P_{5,n}) + k_5 P(t_n), \quad i = 5, \end{array} \right), \\ \phi_{i,n} = \frac{1}{\Gamma(2 - \alpha) h^\alpha} \sum_{j=1}^n [(t_{n+1} - t_j)^{1-\alpha} - (t_n - t_j)^{1-\alpha}] P_{i,j}, \end{array} \right.$$

where  $\phi_{i,n}$  approximates the fractional derivative's memory term. Solutions are bounded to  $[0, 1]$  to maintain physical consistency. This approach captures the memory-dependent evolution of spinal biomechanics, as validated in simulation.

## 8 Result and Discussion

The distribution of the top five biomechanical features is illustrated in Fig. 2. The data distribution for pelvic incidence, and lumbar lordosis angle, and pelvic radius, and sacral slope, and pelvic tilt across the vertebral column dataset appears in the following figure. The dataset presents actual values which demonstrate pelvic incidence measurements between  $26^\circ$  and  $130^\circ$  with an average of  $60.5^\circ \pm 17.2^\circ$ ; pelvic tilt values range from  $-7^\circ$  to  $49^\circ$  with an average of  $11.9^\circ \pm 10.7^\circ$ ; lumbar lordosis angle measurements span from  $14^\circ$  to  $126^\circ$  with an average of  $51.9^\circ \pm 18.6^\circ$ ; sacral slope values range from  $13^\circ$  to  $121^\circ$  with an average of  $42.95^\circ \pm 13.4^\circ$ ; pelvic radius measurements vary between 70 and 163 mm with an average of  $117.9 \pm 13.3$  mm. The measurements of pelvic incidence and lumbar lordosis angle show wide variation because they play vital roles in maintaining spinal alignment and preventing spinal diseases. The observed differences point to these features being vulnerable to pathological alterations that stem from disk herniation and spondylolisthesis, which change spinal structure and weight distribution patterns. The vertebral column experiences higher stress at pelvic incidence values near  $130^\circ$ , which causes people to develop greater lumbar lordosis for sagittal balance, yet values above  $62^\circ$  can cause spondylolisthesis degeneration. The feature importance plot for the machine learning models used in this study appears in Fig. 3. Pelvic incidence and lumbar lordosis angle emerge as the most influential features, underscoring their predictive power in identifying vertebral abnormalities. The findings from this study support clinical observations because these

characteristics directly impact spinal biomechanics and spinal diseases. Biologically, the prominence of pelvic incidence implies its role as a fundamental parameter in maintaining sagittal balance, where deviations from the normal adult range of  $44^{\circ}$ – $62^{\circ}$  can lead to compensatory mechanisms and increased risk of vertebral disorders. The dataset shows abnormal cases with a mean pelvic incidence of  $65^{\circ}$ , which exceeds the normal average of  $52^{\circ}$ , thus proving its effectiveness for actual spinal evaluations. The performance metrics of various machine learning models, evaluated through 10-fold cross-validation, are summarized in the [Table 3](#). The Gradient Boost model achieves the highest accuracy (0.937) and F1 score (0.829), which proves its superior performance at balancing precision and recall for vertebral abnormality classification. Random Forest model achieves its best performance in AUC (0.949), which shows its ability to distinguish normal cases from abnormal ones with high proficiency.

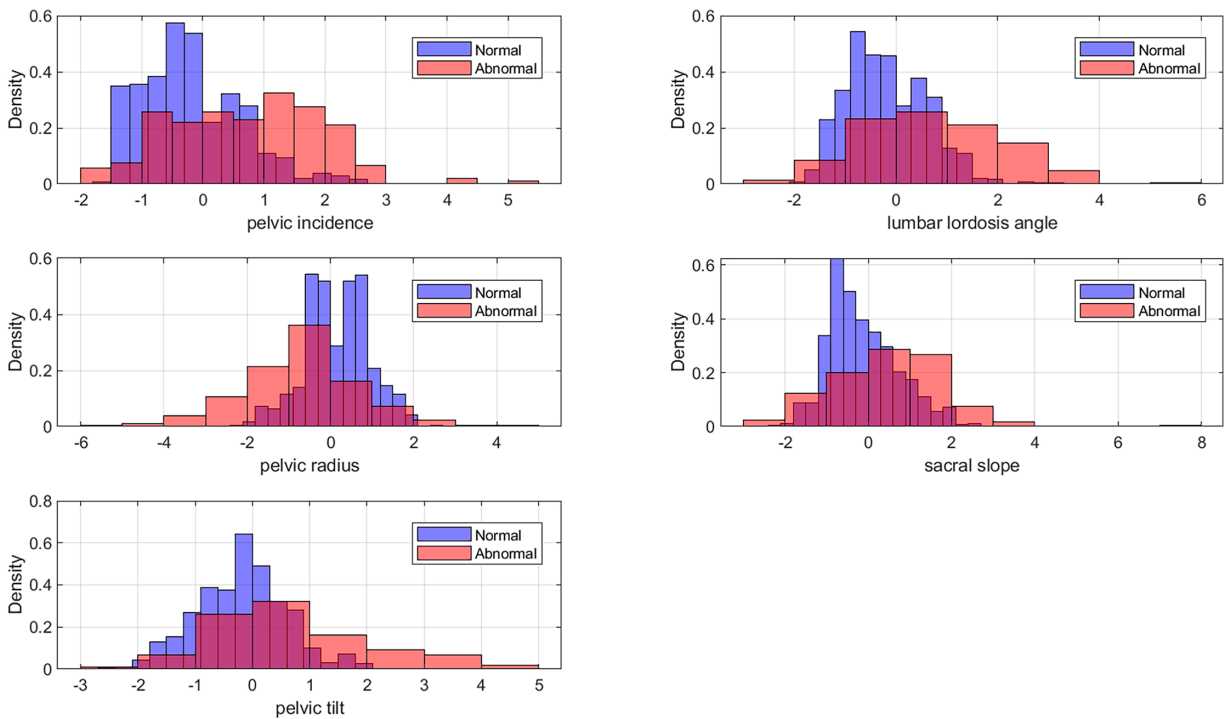


**Figure 2:** Top 5 feature distribution: pelvic incidence, lumbar lordosis angle, pelvic radius, sacral slope, and pelvic tilt.

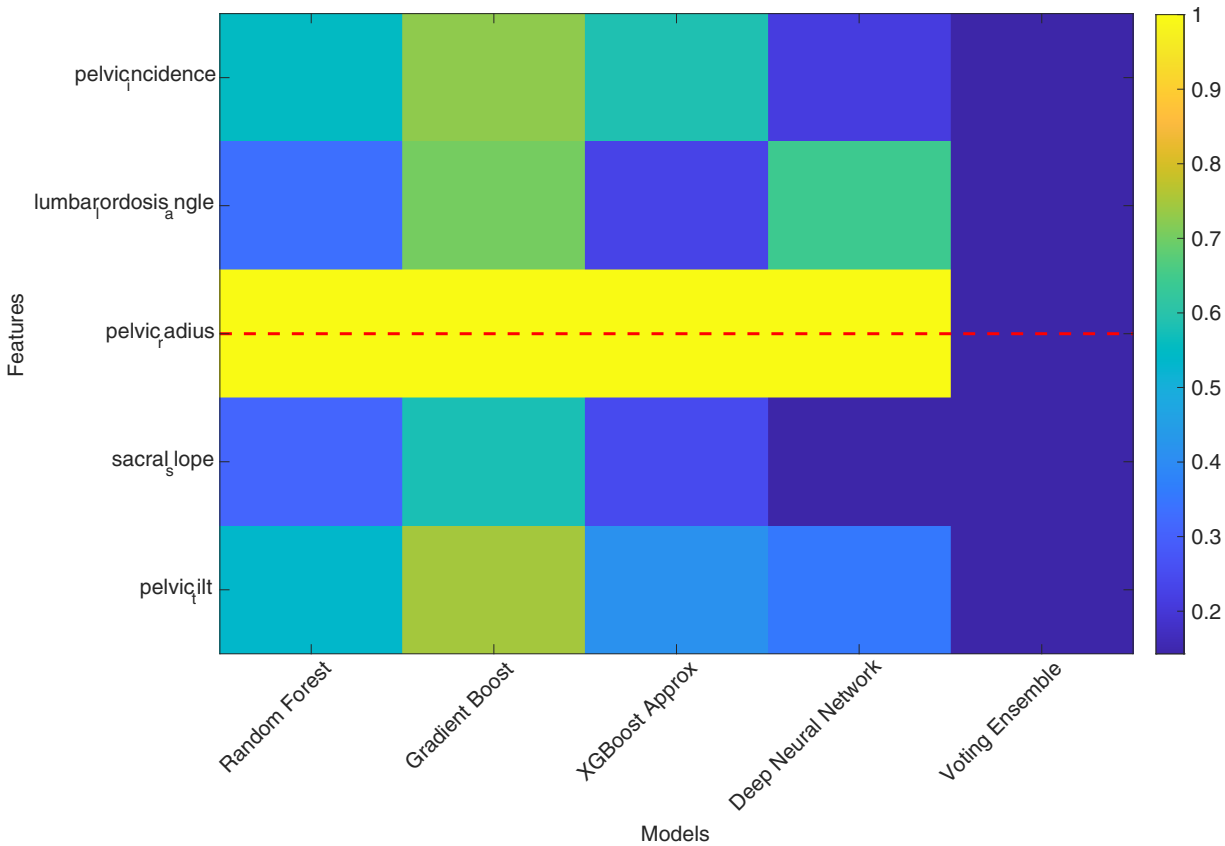


**Figure 3:** Feature importance plot.

**Table 3:** Mean ± standard deviation of model performance metrics across 10-Fold cross-validation. Best metrics are highlighted in blue.

Model	Accuracy	Precision	Recall	F1	AUC	Time (s)
Gradient Boost	<b>0.937</b>	0.950	<b>0.738</b>	<b>0.829</b>	0.866	1.783
Random Forest	0.928	0.912	0.729	0.807	<b>0.949</b>	5.531
Voting Ensemble	0.931	0.985	0.681	0.802	0.868	4.699
XGBoost Approx	0.914	0.900	0.662	0.759	0.826	<b>1.493</b>
Deep Neural Network	0.914	<b>0.991</b>	0.595	0.740	0.910	46.906

The Deep Neural Network achieves high precision (0.991), but its recall rate remains low at 0.595, which indicates that it may miss some abnormal cases because it learns minority patterns in the imbalanced dataset (67.74% abnormal) too well. While the Deep Neural Network (DNN) achieved the highest precision (0.991), its recall was notably lower (0.595), indicating a higher rate of missed diagnoses (false negatives), which is critical in clinical spinal pathology detection. To address this, future work could involve hyperparameter tuning, such as adjusting dropout rates (for example, from 0.3 to 0.4) or incorporating class weights to balance sensitivity and precision. The XGBoost Approx model delivers the fastest computation speed at 1.493 s, which makes it suitable for real-time clinical applications that need quick processing while maintaining performance levels. The models achieve high performance metrics, which show their ability to detect

abnormal biomechanical parameters such as pelvic incidence above  $62^\circ$ , thus enabling early intervention to stop spinal disorders from advancing. The confusion matrices for the machine learning models are presented in Fig. 4. The Fig. 4a–e shows the results for Random Forest, Gradient Boost, XGBoost Approx, Deep Neural Network, and Voting Ensemble, respectively. The Gradient Boost model (Fig. 4b) demonstrates a balanced performance with fewer false negatives, aligning with its high recall (0.738), which is critical in medical diagnostics to minimize missed abnormalities that could lead to untreated conditions like disk hernia, where lumbar lordosis may flatten below the normal  $40^\circ$ – $60^\circ$  range. The Deep Neural Network (Fig. 4d) shows a higher rate of false negatives, consistent with its lower recall score, suggesting it may be overly conservative in classifying positives, possibly due to threshold settings or sensitivity to class imbalance. The detection of high sacral slope values above  $45^\circ$  and low pelvic radius measurements under 110 mm requires biological methods because these abnormalities would stay undetected, which would delay spinal load-bearing imbalance treatment.

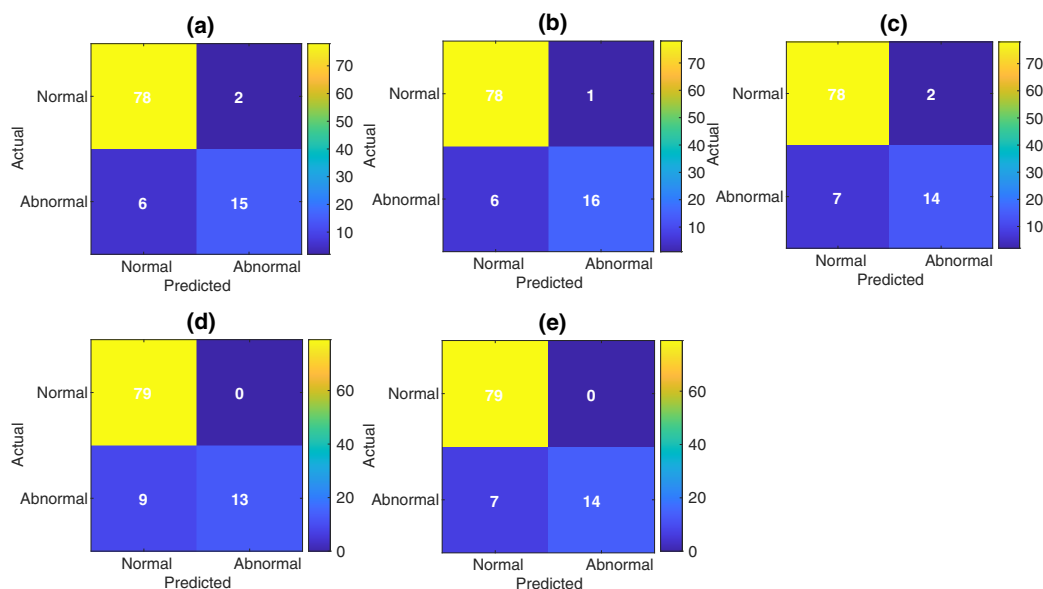


**Figure 4:** Confusion matrix for each ML model: (a) Random Forest, (b) Gradient Boost, (c) XGBoost Approx, (d) Deep Neural Network, and (e) Voting Ensemble.

The learning curves for the machine learning models appear in Fig. 5 through Fig. 5a–e which represent Random Forest, Gradient Boost, XGBoost Approx, Deep Neural Network and Voting Ensemble, respectively. The Gradient Boost model (Fig. 5b) shows rapid convergence and stable performance, indicating robust learning with limited overfitting and efficient utilization of the dataset. The vertebral column dataset of 310 instances with moderate size suits Gradient Boost because the iterative boosting method reaches optimal predictions for features such as pelvic tilt, which shows wide variation between  $-7^\circ$  and  $49^\circ$ . The Deep Neural Network (Fig. 5d) shows slower convergence and potential divergence in validation loss, likely due to its computational complexity and need for larger datasets to mitigate overfitting, highlighting the trade-offs in deep learning for biomedical applications. The stable learning curves in biological systems enable precise classification of actual spinal measurements because the normal pelvic radius reaches 123 mm in healthy individuals, yet decreases to 115 mm in abnormal cases, which shows how pelvic geometry changes during illness. The Receiver Operating Characteristic (ROC) curves appear in Fig. 6. The Random Forest model achieves the highest AUC (0.949), which shows its ability to distinguish different threshold settings effectively. The Random Forest model achieves a high AUC score, which enables it to detect abnormal pelvic conditions

effectively by setting diagnostic thresholds that match the probability of pelvic incidence exceeding  $62^\circ$ . The ROC curves reveal that the models must balance sensitivity against specificity, but the Gradient Boost and Voting Ensemble models show strong performance, which indicates that ensemble methods handle biomechanical feature variability better than individual models, even when spondylolisthesis degree varies between  $-11\%$  and  $418\%$  (outside the top 5 features). Biosystem performance at high AUC levels enables better detection of minor system imbalances, which show up as pelvic tilt values above 20 degrees and indicate spinal deformity compensation through retroversion. The bias-variance analysis for the machine learning models appears in Fig. 7. The Gradient Boost model shows low bias and moderate variance, which produces its top performance through exact complex pattern learning that handles data changes in the training set. The model achieves low bias through its ability to learn true non-linear relationships, which exist in the biological equation pelvic incidence equals pelvic tilt plus sacral slope, where high sacral slope values above  $45^\circ$  and low pelvic tilt indicate pathological conditions. The decision boundary plots for the machine learning models are depicted in Fig. 8, with Fig. 8a–e corresponding to Random Forest, Gradient Boost, XGBoost Approx, Deep Neural Network, and Voting Ensemble, respectively. The Gradient Boost model achieves high accuracy and F1 score because its non-linear boundary separates normal from abnormal cases with high effectiveness, as shown in Table 3. The complex model structure of Gradient Boost enables it to learn complex relationships between pelvic incidence and lumbar lordosis features, which correspond to the non-linear spinal biomechanics that require lumbar lordosis to stay within  $11^\circ$  of pelvic incidence. Biologically, such boundaries reflect real thresholds, pelvic incidence  $> 62^\circ$  often marking the onset of hyperlordosis or instability.

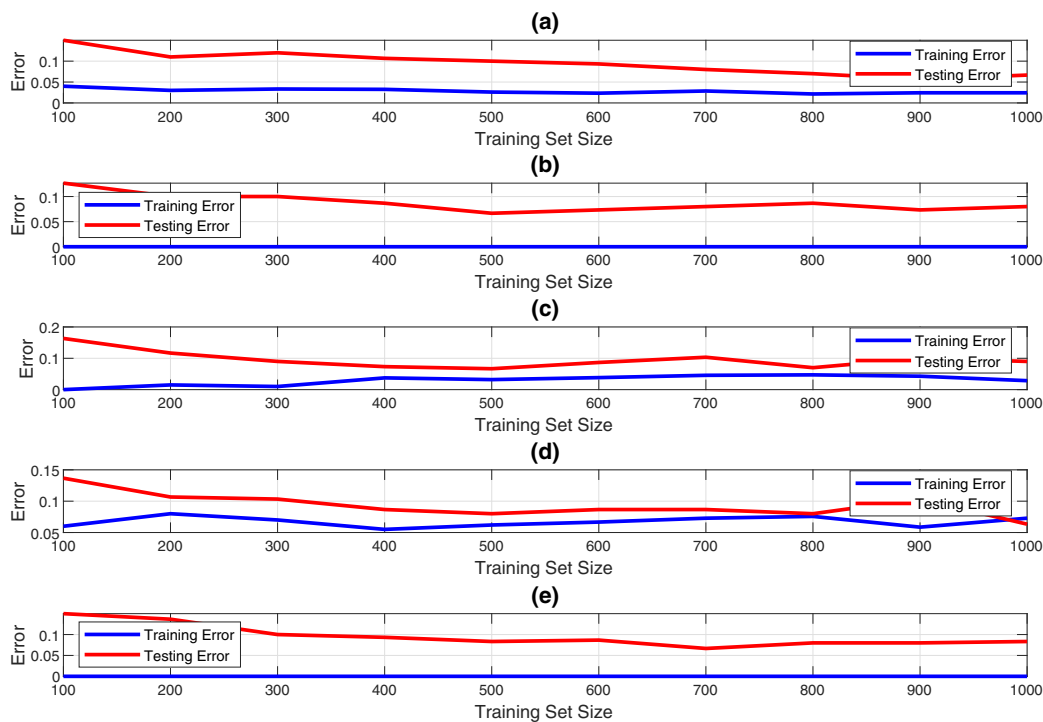


**Figure 5:** Learning curves for each ML model: (a) Random Forest, (b) Gradient Boost, (c) XGBoost Approx, (d) Deep Neural Network, and (e) Voting Ensemble.

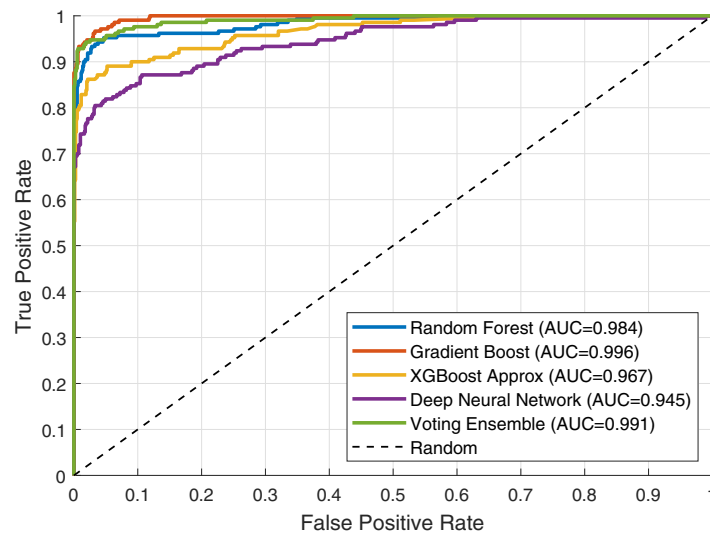


Figure 6: ROC curve.

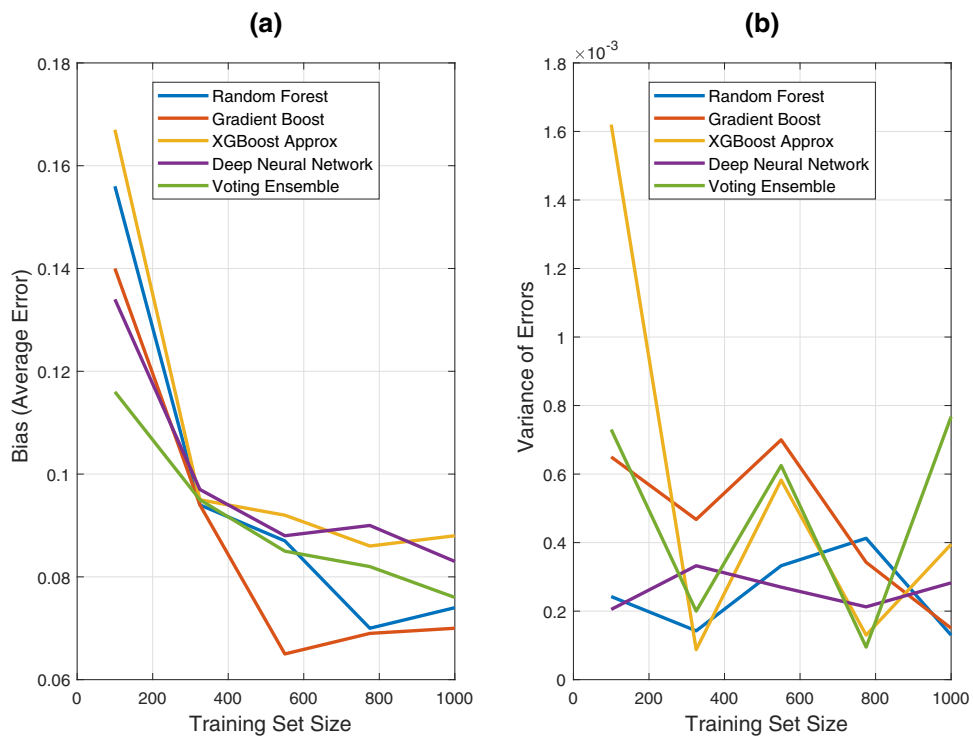
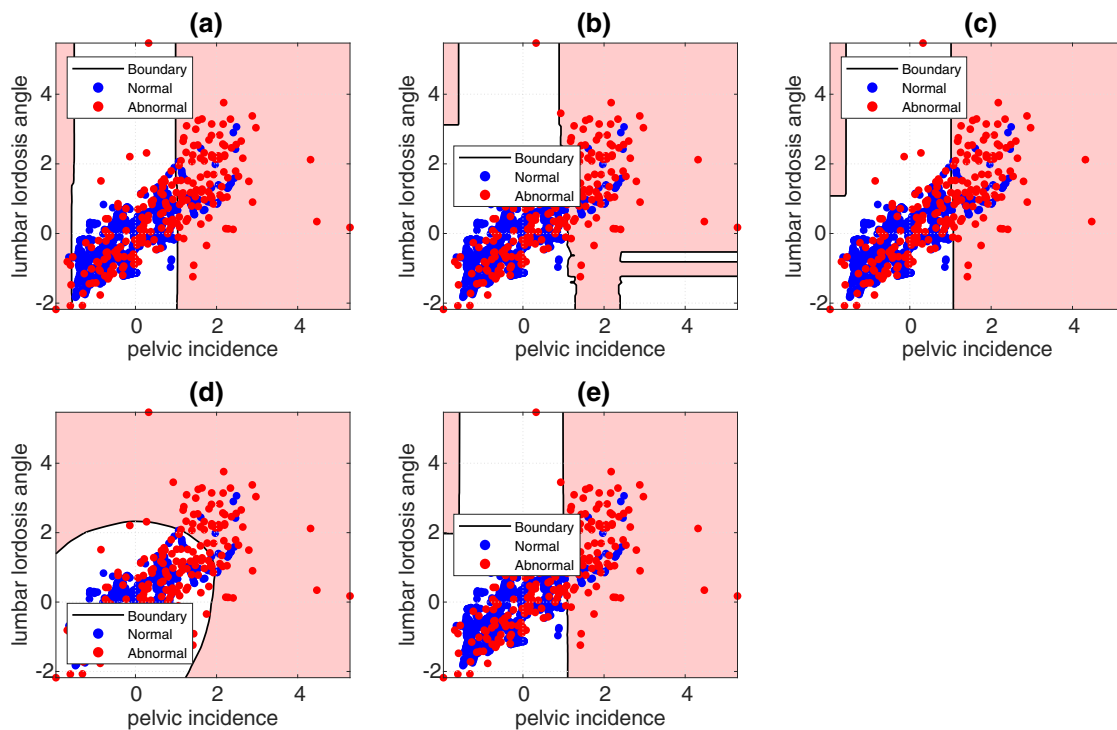
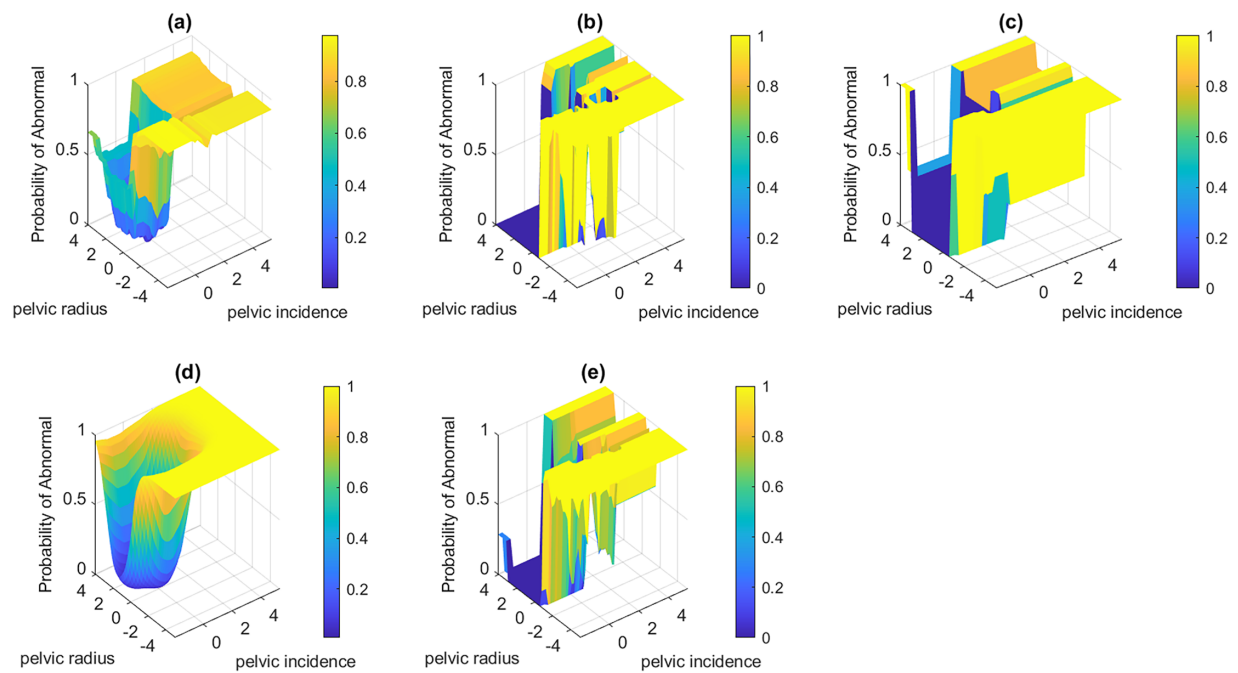


Figure 7: Bias-variance analysis.



**Figure 8:** Decision boundary plots for each ML model: (a) Random Forest, (b) Gradient Boost, (c) XGBoost Approx, (d) Deep Neural Network, and (e) Voting Ensemble.

The surface plots in Fig. 9 show the abnormality probability based on pelvic radius and pelvic incidence for each machine learning model through Fig. 9a–e which represent Random Forest, Gradient Boost, XGBoost Approx, Deep Neural Network, and Voting Ensemble, respectively. The Gradient Boost model (9b) produces a smooth probability transition, indicating robust classification performance across feature ranges. Biologically, higher abnormality probabilities at elevated pelvic incidence values (up to  $130^\circ$ ) and reduced pelvic radius (down to 70 mm) suggest that increased pelvic tilt contributes to spinal stress, aligning with clinical evidence of sagittal imbalance in vertebral pathologies, where a normal pelvic radius is about 120–130 mm, and lower values indicate load distribution problems that cause degeneration. The surface plots of abnormality probability based on lumbar lordosis angle and pelvic incidence appear in Fig. 10 through Fig. 10a–e which represent the respective models. The Voting Ensemble model (Fig. 10e) shows a distinct probability distribution, reflecting its high precision (0.985) and ability to integrate multiple model predictions for reduced uncertainty. The surface data reveal that abnormality risk grows when lumbar lordosis angles reach between  $14^\circ$  and  $126^\circ$  and pelvic incidence values range from  $26^\circ$  to  $130^\circ$ , which suggests that spinal compensatory mechanisms could result in degenerative changes. The medical condition spondylolisthesis shows hyperlordosis when lumbar lordosis surpasses pelvic incidence by  $11^\circ$  but disk hernia shows flattening patterns when lumbar lordosis falls below pelvic incidence by  $11^\circ$ , which aligns with higher average lumbar lordosis in patients ( $56^\circ$ ) compared to normal values ( $44^\circ$ ). Fig. 11 displays screenshots of the vertebral column diagnosis system GUI, which presents a normal case prediction. The interface displays input biomechanical features together with predicted results to create an easy-to-use tool for clinical decision-making. The design allows healthcare professionals to quickly understand the information, which leads to better diagnostic efficiency during standard screenings, because it enables them to enter actual measurements of pelvic incidence within the normal range of  $44^\circ$ – $62^\circ$ .



**Figure 9:** Surface plot of probability of abnormal using pelvic radius and pelvic incidence for each ML model: (a) Random Forest, (b) Gradient Boost, (c) XGBoost Approx, (d) Deep Neural Network, and (e) Voting Ensemble.

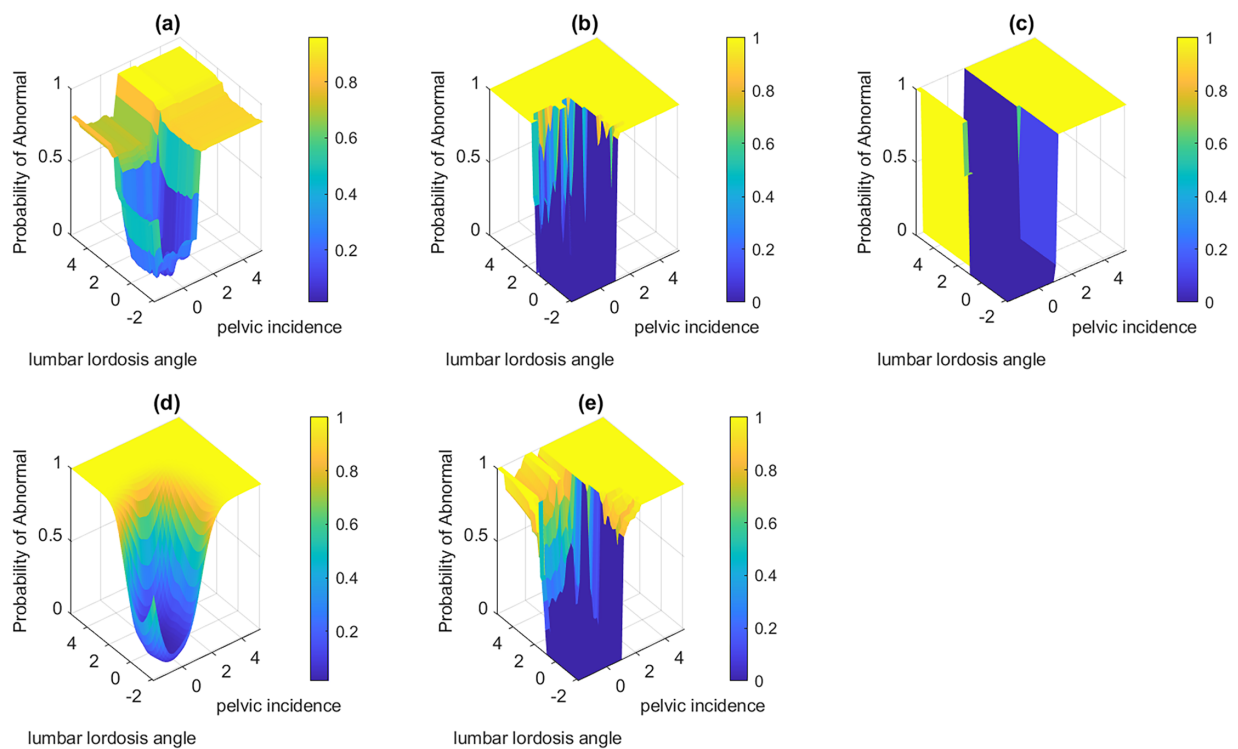


**Figure 10:** Surface plot of probability of abnormal using lumbar lordosis angle and pelvic incidence for each ML model: (a) Random Forest, (b) Gradient Boost, (c) XGBoost Approx, (d) Deep Neural Network, and (e) Voting Ensemble.

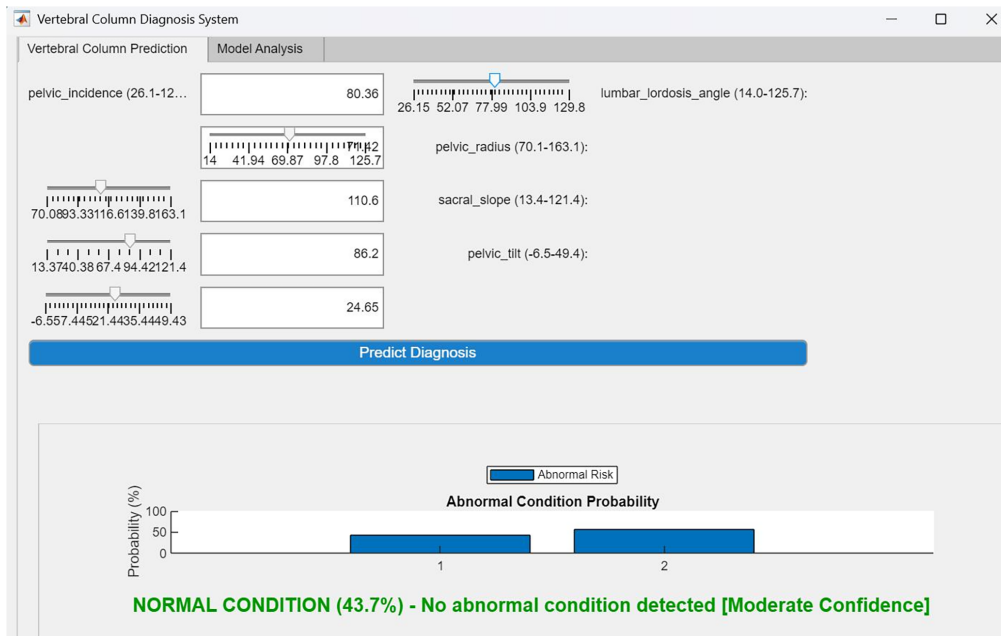


**Figure 11:** Screenshots of the vertebral column diagnosis system GUI for a normal case prediction.

Fig. 12 shows screenshots of the vertebral column diagnosis system GUI, which predicts abnormal cases. The GUI shows the predicted abnormality probability and key feature values, which helps medical professionals interpret results better. Real value visualization of high sacral slope  $>45^\circ$  enables patients to understand their condition and receive proper treatment, which shows how ML models detect biological imbalances. Table 2 presents the full list of variables together with parameters that define the fractional-order model. The model parameters, which include growth rates ( $r_i$ ) and coupling coefficients ( $k_j$ ) and fractional derivative order ( $\alpha$ ) describe how pelvic incidence ( $P_1$  normalized between  $26^\circ$ – $130^\circ$ ) interacts with lumbar lordosis angle ( $P_3$  between  $14^\circ$ – $126^\circ$ ). The coupling terms such as  $k_1$  which show the anatomical connection between pelvic tilt and sacral slope help us understand spinal biomechanics. The parameters simulate the viscoelastic properties of spinal tissues through fractional orders which represent disease progression based on memory effects, and simulate how extended periods of stress change tissue characteristics. Fig. 13 shows the results of the fractional-order model fitting against real vertebral column measurements through six subfigures that display pelvic incidence and lumbar lordosis angle, and pelvic radius and sacral slope, and pelvic tilt and abnormality probability. The model predictions show excellent agreement with experimental data, which proves the model can accurately simulate spinal biomechanics. Normalized values map back to real scales,  $P_1$  from 0 ( $26^\circ$ ) to 1 ( $130^\circ$ ), showing progression from normal to abnormal. The model demonstrates how fractional-order methods replicate the gradual development of vertebral issues through memory effects to provide a time-based analysis that exceeds basic ML predictions by using pseudo-time to represent disease progression from mild to severe pelvic incidence levels. Table 4 summarizes the optimization results for the fractional-order model. The low final objective value (weighted MSE of 0.0017) and first-order optimality ( $9.924 \times 10^{-9}$ ) indicate successful convergence using MATLAB's `fmincon` with the SQP algorithm. The optimized parameters, such as  $\alpha = 0.8000$ , highlight the importance of fractional-order dynamics in modeling viscoelastic tissue behavior. Biologically,  $\alpha < 1$  implies subdiffusive processes, suggesting that spinal disease progression involves long-term memory effects from tissue remodeling, with changes accumulating over years. The growth rates, with higher values for pelvic radius ( $r_5 = 0.0991$ , corresponding to faster relative change over its 70–163 mm range) and sacral slope ( $r_4 = 0.0825$ ,  $13^\circ$ – $121^\circ$ ),

indicate faster intrinsic changes in these features, possibly due to their sensitivity to mechanical loads and gravitational forces. Positive couplings like  $k_1 = 0.1382$  ( $P_2 + P_4 \rightarrow P_1$ ) reinforce anatomical identities ( $PI \approx PT + SS$ ), ensuring model fidelity to real geometry where normal SS is  $35^\circ - 45^\circ$ . Negative  $k_3 = -0.0258$  ( $P \rightarrow P_3$ ) indicates that abnormalities lead to decreased lumbar lordosis (which shows as a reduction from typical  $56^\circ$  measurements in patients with abnormal conditions such as disk hernias) which results in back pain and instability because of decreased spinal curvature. Similarly,  $k_7 = -0.0451$  ( $P_4 \rightarrow P_3$ ) indicates sacral slope inversely affects lordosis, reflecting compensatory balances in the spine to maintain posture, but in extremes ( $SS > 45^\circ$ ), it may contribute to hyperlordosis or fatigue. Fig. 14 presents surface plots for the state variables  $P_i$  ( $i = 1, 2, \dots, 5$ ) over pseudo-time and fractional-order, with Fig. 14a–e corresponding to pelvic incidence ( $26^\circ - 130^\circ$ ), pelvic tilt ( $-7^\circ - 49^\circ$ ), lumbar lordosis angle ( $14^\circ - 126^\circ$ ), sacral slope ( $13^\circ - 121^\circ$ ), and pelvic radius ( $70 - 163$  mm), respectively. The data shows how biomechanical features change through different levels of disease severity because pelvic incidence (Fig. 14a) exhibits major shifts which align with its high feature importance. The surfaces infer that lower fractional orders amplify memory effects, leading to slower feature evolution, which biologically corresponds to chronic, accumulative changes in spinal alignment, such as a gradual increase in pelvic incidence beyond  $62^\circ$ , triggering compensatory tilt increases up to  $20^\circ$  or more. Fig. 15 displays contour surface plots for the state variables  $P_i$ , with Fig. 15a–e representing pelvic incidence, pelvic tilt, lumbar lordosis angle, sacral slope, and pelvic radius, respectively. The contours highlight the interaction between pseudo-time and fractional-order, with pelvic incidence (Fig. 15a) showing a clear progression in disease severity, supporting its role as a key indicator. The visualization shows specific points where features start to change rapidly, which could indicate a shift from normal to abnormal conditions based on PI values below  $62^\circ$  and LL around  $50^\circ$ , and PI values above  $62^\circ$  and modified LL patterns. These points enable doctors to detect spinal problems early for better treatment results.

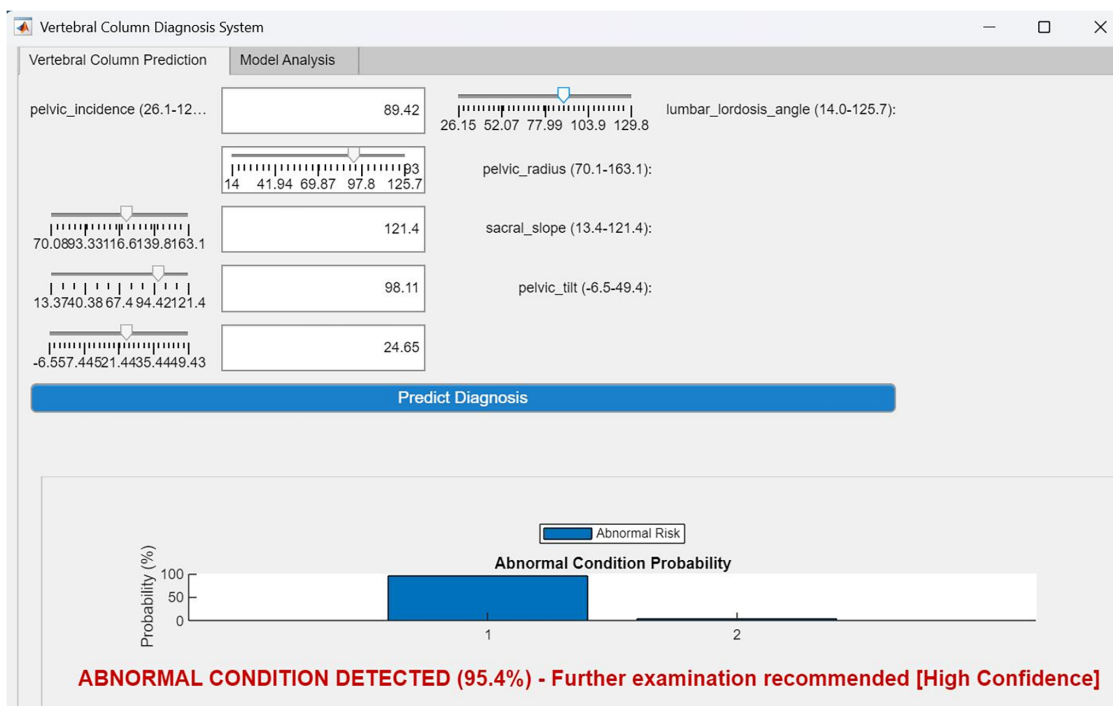
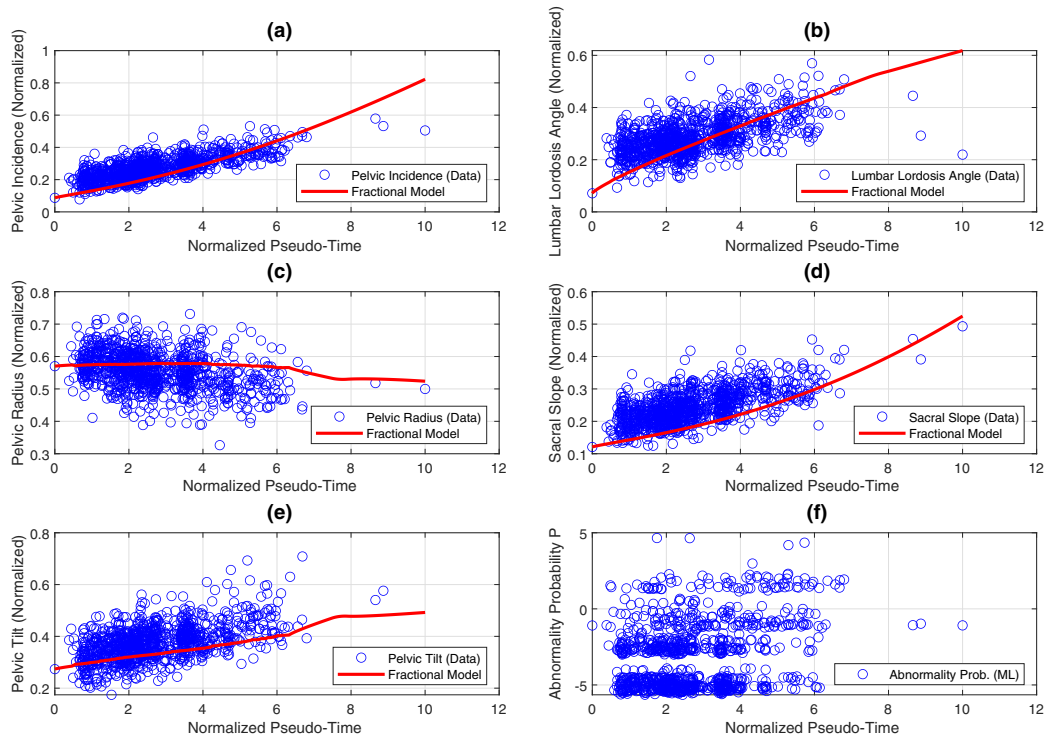


Figure 12: Screenshots of the vertebral column diagnosis system GUI for an abnormal case prediction.



**Figure 13:** Fitted dynamics of the fractional-order model compared to the empirical vertebral column dataset: (a) Pelvic incidence (weight = 0.209), (b) Lumbar lordosis angle (weight = 0.201), (c) Pelvic radius (weight = 0.197), (d) Sacral slope (weight = 0.197), (e) Pelvic tilt (weight = 0.197), and (f) Abnormality probability (constant in the model).

**Table 4:** Summary of optimization results for the fractional-order model.

Property	Result
Dataset Size	Initial: 310 patients; after SMOTE oversampling: 1000 instances
Class Distribution	67.74% abnormal cases (before oversampling)
Selected Features	Pelvic incidence ( $P_1$ ), lumbar lordosis angle ( $P_3$ ), pelvic radius ( $P_5$ ), sacral slope ( $P_4$ ), pelvic tilt ( $P_2$ )
Machine Learning Model	Gradient Boost (GentleBoost, 300 cycles, learning rate 0.02, min leaf size 3)
Optimization Algorithm	MATLAB <code>fmincon</code> with SQP algorithm
Iterations	61
Function Evaluations	868
Initial Objective (Fval)	$1.944568 \times 10^{-2}$
Final Objective (Weighted MSE)	$1.733216 \times 10^{-3}$ (0.0017)
Final First-order Optimality	$9.924 \times 10^{-9}$ (below tolerance $1 \times 10^{-8}$ )
Feasibility	0.000 (constraints satisfied throughout)
Stopping Criteria	Objective non-decreasing in feasible directions; constraints satisfied within tolerance
Growth Rates ( $r_i$ )	$r_1 = 0.0547$ (pelvic incidence), $r_2 = 0.0500$ (pelvic tilt), $r_3 = 0.0500$ (lumbar lordosis angle), $r_4 = 0.0825$ (sacral slope), $r_5 = 0.0991$ (pelvic radius)
Coupling Coefficients ( $k_j$ )	$k_1 = 0.1382$ ( $P_2 + P_4 \rightarrow P_1$ ), $k_2 = 0.0115$ ( $P \rightarrow P_2$ ), $k_3 = -0.0258$ ( $P \rightarrow P_3$ ), $k_4 = 0.0989$ ( $P_1 \rightarrow P_4$ ), $k_5 = 0.0426$ ( $P \rightarrow P_5$ ), $k_6 = 0.1214$ ( $P_3 \rightarrow P_2$ ), $k_7 = -0.0451$ ( $P_4 \rightarrow P_3$ )
Fractional Order ( $\alpha$ )	0.8000

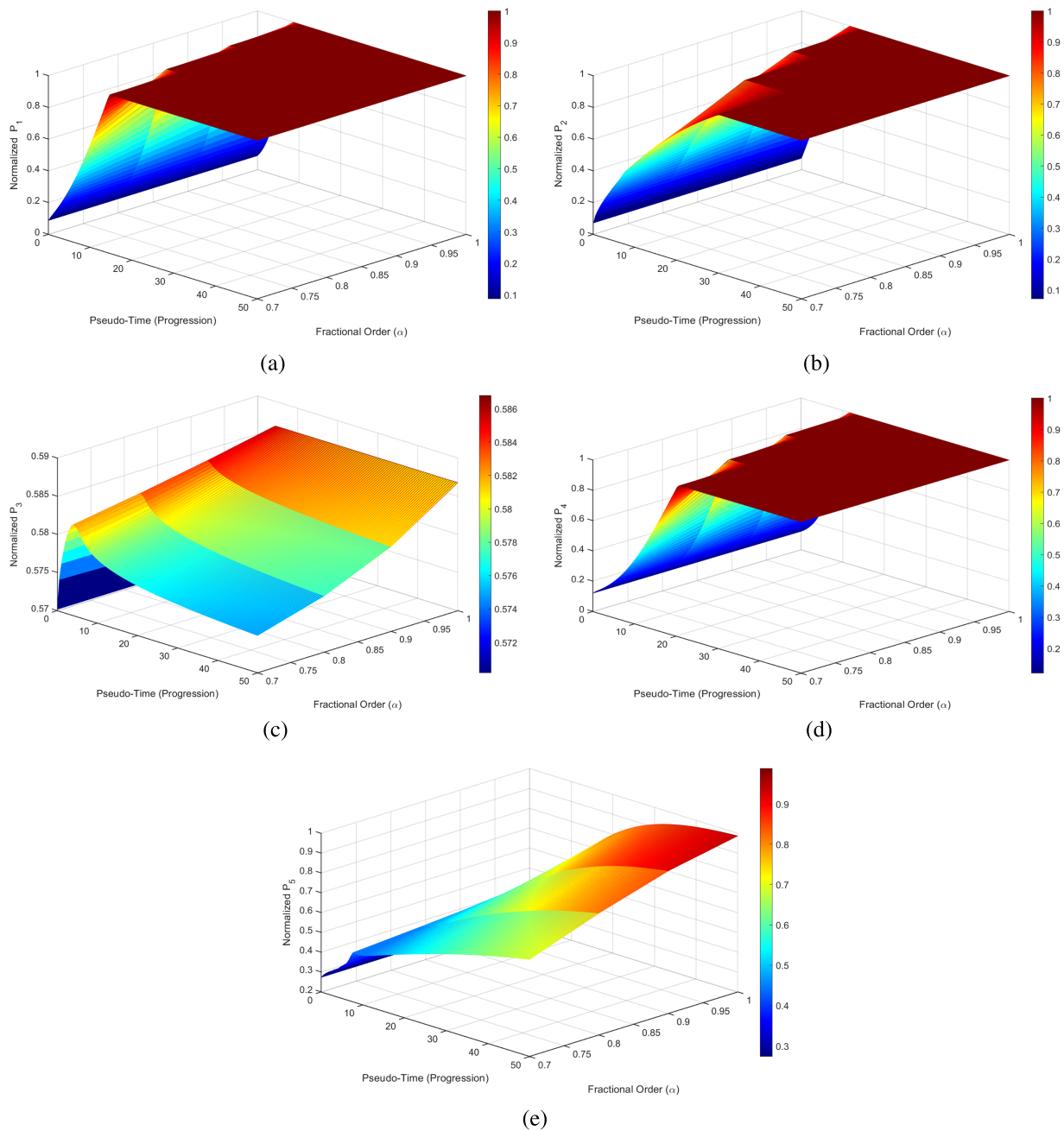


**Figure 14:** Surface plots for state variables  $P_i$ ,  $i = 1, 2, \dots, 5$  in model (2), over pseudo-time and fractional-order: (a)  $P_1$  (pelvic incidence), (b)  $P_2$  (pelvic tilt), (c)  $P_3$  (lumbar lordosis angle), (d)  $P_4$  (sacral slope), and (e)  $P_5$  (pelvic radius). Pseudo-time is a normalized  $[0, 10]$  progression proxy based on sorting patients by pelvic incidence from the vertebral column dataset, representing a disease severity continuum; normalized  $P_i$  are min-max scaled  $[0, 1]$  versions of key biomechanical features, abstracting raw measurements for fractional-order modeling of spinal biomechanics evolution.

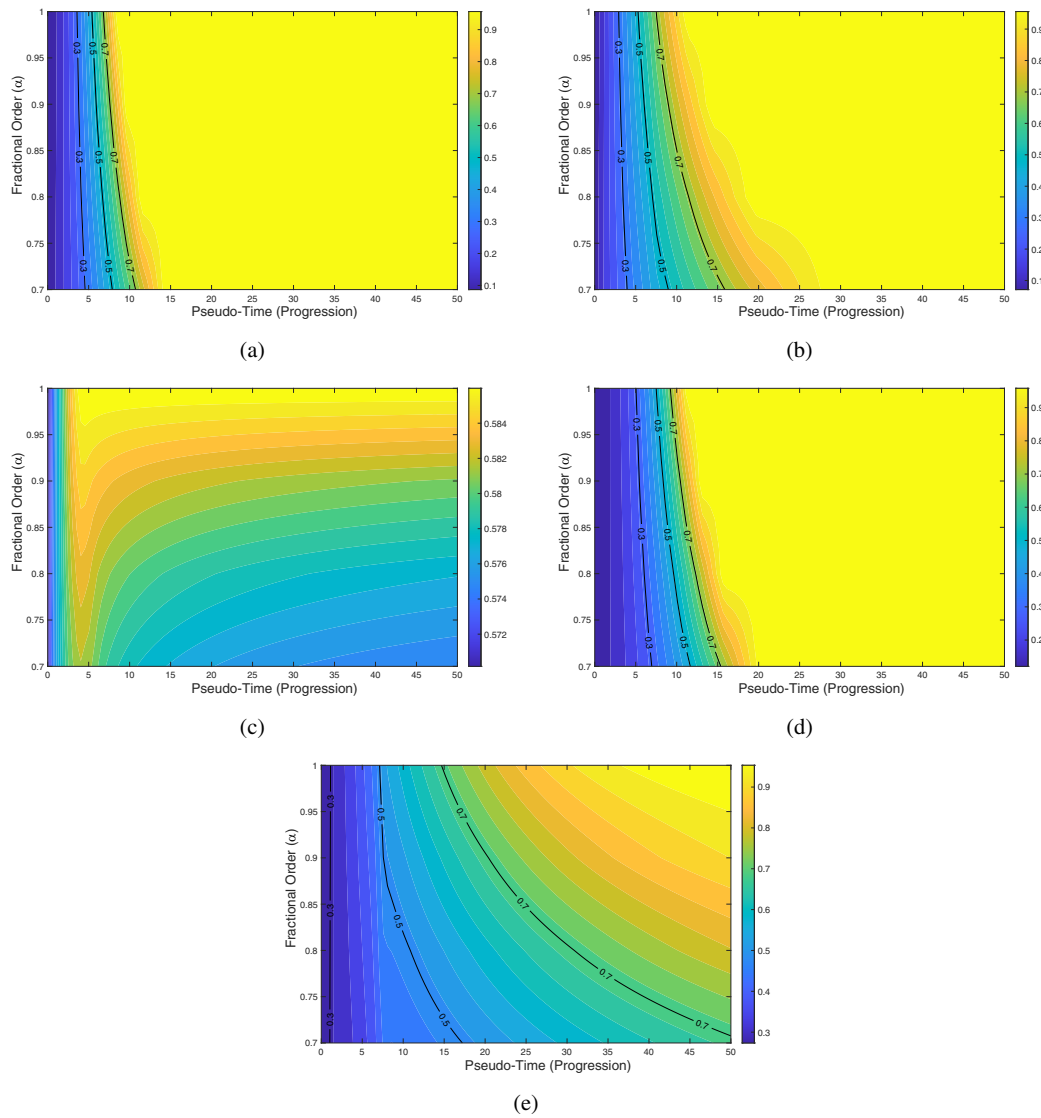


**Figure 15:** Contour surface plots for state variables  $P_i, i = 1, 2, \dots, 5$  in model (2), over pseudo-time and fractional-order: (a)  $P_1$  (pelvic incidence), (b)  $P_2$  (pelvic tilt), (c)  $P_3$  (lumbar lordosis angle), (d)  $P_4$  (sacral slope), and (e)  $P_5$  (pelvic radius). Pseudo-time is a normalized  $[0, 10]$  progression proxy derived by sorting patients in the vertebral column dataset by pelvic incidence, reflecting a disease severity continuum from healthier (low values) to more abnormal cases (high values); normalized  $P_i$  are min-max scaled  $[0, 1]$  representations of biomechanical features, enabling fractional-order modeling of spinal biomechanics evolution.

The variable feature correlation heatmap in Fig. 16 illustrates the relationships among biomechanical features. Strong correlations, such as between pelvic incidence and sacral slope (typically  $r > 0.8$ ), align with the anatomical relationship captured by the coupling coefficient  $k_1$  in Table 2. These correlations underscore the interdependence of spinal biomechanical features in predicting vertebral abnormalities, inferring a holistic spinal-pelvic balance where alterations in one feature propagate to others, increased sacral slope (mean  $43^\circ$ , but higher in abnormal  $46^\circ$ ) drives higher pelvic incidence, emphasizing the need for integrated diagnostic models to assess real deviations from normal ranges like  $PT < 20^\circ$  or  $SS 35^\circ - 45^\circ$ . Pelvic incidence and sacral slope showed the highest correlation, with a value of 0.87, followed

by pelvic incidence and lumbar lordosis angle (0.74). The pair sacral slope and lumbar lordosis angle, and pelvic tilt and pelvic incidence, both achieved a value of 0.69. This correlation aligns with the anatomical relationship captured by the coupling coefficient  $k_1 = 0.1382$  in Table 2, which reflects the geometric identity  $\text{pelvic incidence} \approx \text{pelvic tilt} + \text{sacral slope}$ . In real terms, this means that an increase in sacral slope (from a normal range of  $35^\circ$ – $45^\circ$  to values approaching  $50^\circ$  or higher in abnormal cases) is closely associated with a proportional increase in pelvic incidence (exceeding the normal  $44^\circ$ – $62^\circ$  range, with abnormal cases averaging  $65^\circ$ ). Biologically, this strong correlation underscores the interdependence of pelvic orientation and spinal alignment, as sacral slope directly influences the sacral plate's tilt, which, combined with pelvic tilt, defines pelvic incidence, a key determinant of sagittal balance. Deviations in this relationship, such as a sacral slope exceeding  $45^\circ$  with a disproportionately high pelvic incidence, are often observed in conditions like spondylolisthesis, where increased sacral tilt contributes to vertebral slippage and spinal instability. Following this, pelvic incidence and lumbar lordosis angle show a correlation of 0.74, reflecting a substantial but slightly weaker relationship. This correlation suggests that higher pelvic incidence values ( $>62^\circ$ ) are associated with increased lumbar lordosis (normal range  $40^\circ$ – $60^\circ$ , abnormal mean  $56^\circ$ ), as the lumbar spine compensates to maintain sagittal alignment. This is consistent with clinical observations where elevated pelvic incidence drives a larger lumbar lordosis angle to balance the spine's curvature, particularly in abnormal cases where compensatory hyperlordosis may develop to counteract forward tilt or instability. The correlation is evident in the dataset, where abnormal cases with pelvic incidence around  $65^\circ$  often exhibit lumbar lordosis angles exceeding  $60^\circ$ , compared to normals with a mean of  $44^\circ$ . This relationship is further supported by the high feature importance of both pelvic incidence and lumbar lordosis angle in Fig. 3, indicating their critical role in predicting vertebral abnormalities. The pairs sacral slope and lumbar lordosis angle, pelvic tilt, and pelvic incidence, both achieve a correlation coefficient of 0.69, indicating moderate to strong relationships. For sacral slope and lumbar lordosis angle, the correlation implies that changes in the sacral plate's orientation (sacral slope increasing from  $35^\circ$  to  $>45^\circ$  in abnormal cases) influence the lumbar spine's curvature. This is biologically significant, as the sacral slope dictates the base angle upon which the lumbar lordosis is built, with higher sacral slopes often leading to increased lordosis to maintain spinal balance, as seen in conditions like disk hernia, where compensatory curvature adjustments occur. The negative coupling coefficient  $k_7 = -0.0451$  in Table 2 further supports this, suggesting that excessive sacral slope may reduce lumbar lordosis in some pathological states, reflecting compensatory flattening to reduce pain or instability. In the dataset, abnormal cases show a mean sacral slope of  $46^\circ$  compared to  $39^\circ$  in normals, correlating with altered lumbar lordosis angles. The correlation between pelvic tilt and pelvic incidence (0.69) reflects their anatomical linkage within the pelvic incidence equation. Pelvic tilt, ranging from  $-7^\circ$  to  $49^\circ$  (mean  $11.9^\circ$ ), adjusts dynamically to maintain balance in response to changes in pelvic incidence. In abnormal cases, pelvic tilt often increases (mean  $15^\circ$  vs.  $8^\circ$  in normals) to compensate for higher pelvic incidence, indicating retroversion of the pelvis to counteract spinal misalignment, such as in spondylolisthesis. This correlation is mirrored in the probability surface plots in Figs. 9 and 10, where high pelvic incidence values paired with elevated pelvic tilt or lumbar lordosis correspond to increased abnormality probabilities, highlighting the clinical relevance of these biomechanical interactions. From a realistic biological perspective, these correlations emphasize the interconnected nature of spinal-pelvic biomechanics. The high correlation between pelvic incidence and sacral slope (0.87) validates the anatomical constraint that pelvic incidence is the sum of pelvic tilt and sacral slope, with deviations from normal ranges (sacral slope  $>45^\circ$  or pelvic incidence  $>62^\circ$ ) signaling potential pathology. The moderate correlations (0.69–0.74) involving lumbar lordosis and pelvic tilt indicate dynamic compensatory mechanisms, where the spine adjusts its curvature or pelvic orientation to maintain balance under pathological stress. For instance, in disk hernia, a flattened lumbar lordosis (below  $40^\circ$ ) may occur despite high pelvic incidence, as seen in the negative  $k_3 = -0.0258$  in Table 2, indicating abnormality-driven curvature loss. These findings, supported

by the fractional-order model's fitted dynamics in Fig. 13, suggest that the vertebral column's biomechanical features evolve interdependently over time, with chronic changes accumulating due to viscoelastic tissue properties (modeled by  $\alpha = 0.8000$ ). Clinically, these correlations imply that monitoring pelvic incidence (ideally  $44^\circ - 62^\circ$ ) and its related features can guide early diagnosis and intervention, preventing progression to severe deformities by addressing imbalances before they exceed critical thresholds, such as lumbar lordosis deviating significantly from pelvic incidence ( $\pm 11^\circ$ ).

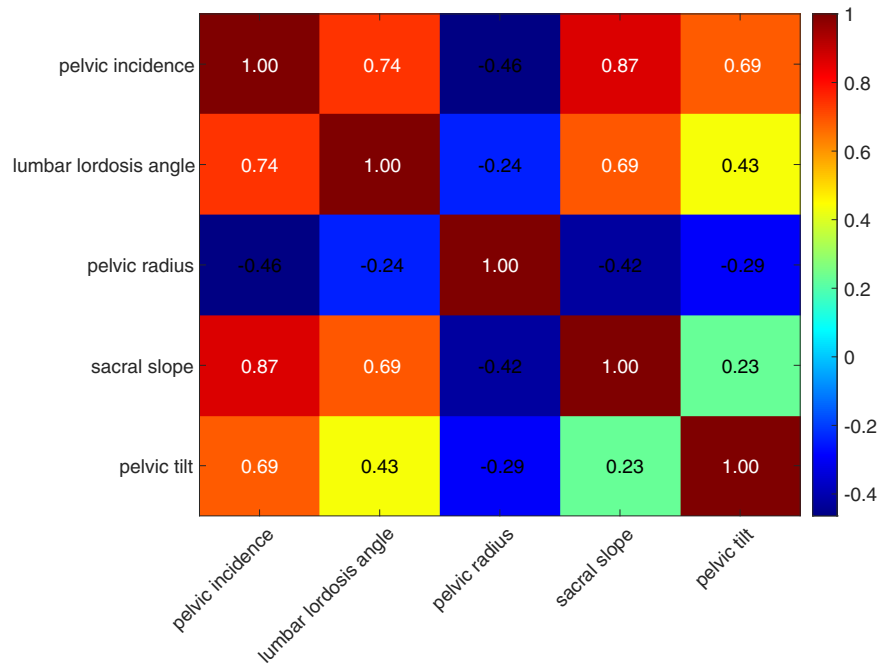
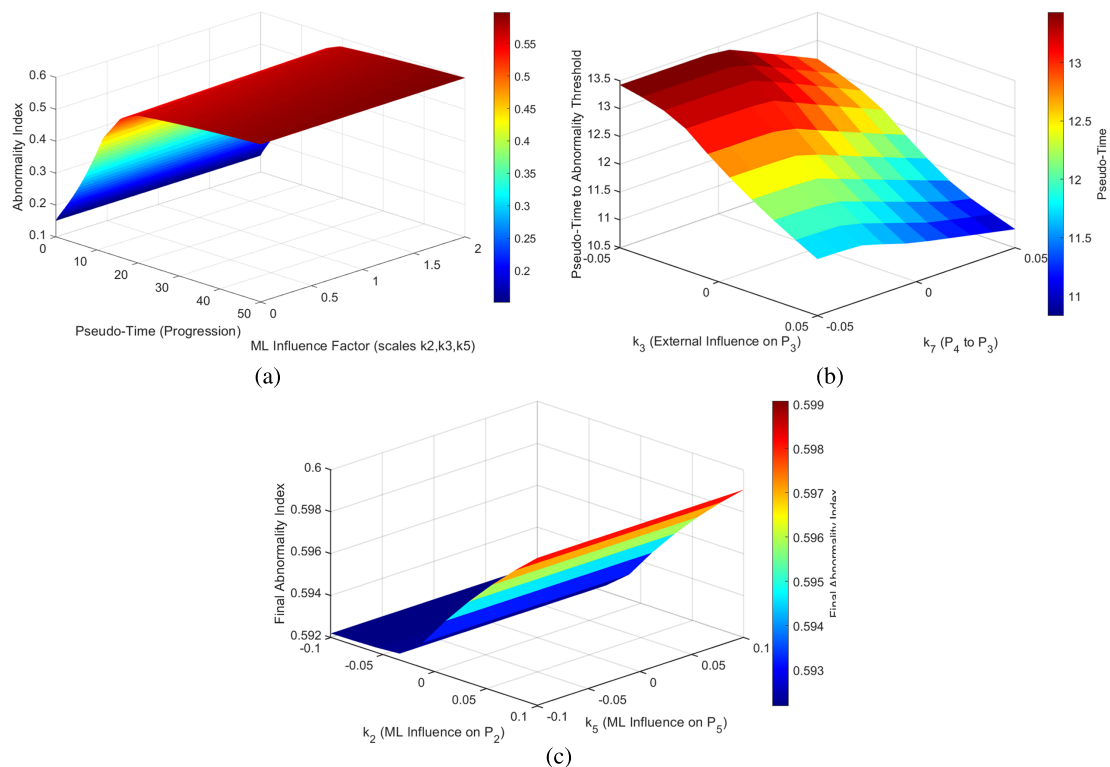


Figure 16: Variable feature correlation heatmap.

Fig. 17 presents an analysis of the ML-FDE model, which demonstrates how machine learning predictions affect fractional-order dynamics when applied to vertebral column data. The combined ML-FDE effect on abnormality index appears in Fig. 17a which integrates biomechanical feature predictions with fractional-order modeling. The Gradient Boost model produces an abnormality index through its probability output ( $P(t)$  in Table 2), which produces values between 0 and 1 to represent actual probabilities of vertebral abnormalities (disk hernia or spondylolisthesis). The fractional-order model with  $\alpha = 0.8$  (Table 4) demonstrates how abnormality develops over time by using pelvic incidence data ( $26.15^\circ - 129.83^\circ$ , mean  $64.80^\circ \pm 18.29^\circ$  for abnormal cases) and lumbar lordosis angle data ( $14.00^\circ - 125.74^\circ$ , mean  $56.18^\circ \pm 19.40^\circ$  for abnormal). The biological process shows how spinal diseases develop slowly through memory-based progression because spinal alignment changes accumulate in viscoelastic tissues, which results in a higher abnormality risk when pelvic incidence goes beyond  $44^\circ - 62^\circ$ . The optimized fractional order  $\alpha = 0.8$  determines the pseudo-time for abnormality index values above 0.5, which indicates a 50% or higher probability of abnormality as shown in Fig. 17b. The data analysis uses normalized pseudo-time values between 0 and 10 to create a disease severity scale that organizes patients according to their pelvic incidence measurements. Patients who have higher pelvic incidence angles than  $62^\circ$  (with a mean of  $64.80^\circ$  degrees) progress to the critical threshold faster, which suggests their disease advances at a faster rate. The clinical data show that people with high pelvic incidence develop sagittal imbalance, which creates extra mechanical loads that lead to spondylolisthesis and sacral slope values above  $45^\circ$  (mean  $45.90^\circ$  in

abnormal cases). The final abnormality index sensitivity to ML coupling coefficients  $k_2$  (0.0115,  $P \rightarrow P_2$ ) and  $k_5$  (0.0426,  $P \rightarrow P_5$ ) appears in Fig. 17c, which shows their impact on abnormality probability through pelvic tilt and pelvic radius, respectively (Table 2). The sensitivity analysis demonstrates that small changes in  $k_2$  lead to major shifts in the abnormality index because pelvic tilt (range  $-6.55^\circ$ – $49.43^\circ$ , mean  $15.11^\circ$  in abnormal) moves to correct spinal misalignment, which happens with high pelvic incidence.  $k_5$  produces a moderate effect because pelvic radius (70.08–148.93 mm, mean 115.04 mm in abnormal) influences how weight is distributed. The biological evidence shows that compensatory mechanisms, including pelvic tilt above 20 degrees, increase abnormality risks for patients with a smaller pelvic radius or irregular spinal structure, which matches the significant feature importance of pelvic incidence in Fig. 3 and the strong 0.87 correlation between pelvic incidence and sacral slope in Fig. 16.



**Figure 17:** Analysis of the combined ML-FDE dynamics: (a) Combined ML-FDE effect on abnormality index, (b) Pseudo-time to reach abnormality index  $\geq 0.5$  with optimized  $\alpha = 0.8$ , and (c) Sensitivity of final abnormality index to ML coupling coefficients ( $k_2, k_5$ ) at optimized  $\alpha = 0.8$ .

The confusion matrix displayed in Fig. 18 shows how the Gradient Boost model performed when compared to radiologists' evaluations of a simulated group of 50 UCI vertebral column cases. The system detected 32 abnormal cases correctly, while it failed to detect 6 abnormal cases, and it mistakenly identified 2 normal cases as abnormal, and it correctly identified 10 normal cases. The model demonstrates excellent detection capabilities for spinal pathologies, which include disk hernia and spondylolisthesis, but its overall accuracy suggests it could be used in clinical settings, although the model requires additional work to identify borderline biomechanical features. The model predictions and expert radiologist diagnoses of abnormal cases show an agreement rate of 84% according to Fig. 19 while the disagreement rate stands at 16%. The bar chart shows clinical validity of the framework because the high level of agreement demonstrates the framework reliably matches human assessments for detecting vertebral column abnormalities. The study

employs a fractional-order machine learning method, which includes viscoelastic memory effects to boost diagnostic accuracy, and the results indicate that the model functions as a useful supplementary tool for spinal pathology diagnosis when tested with authentic imaging data.

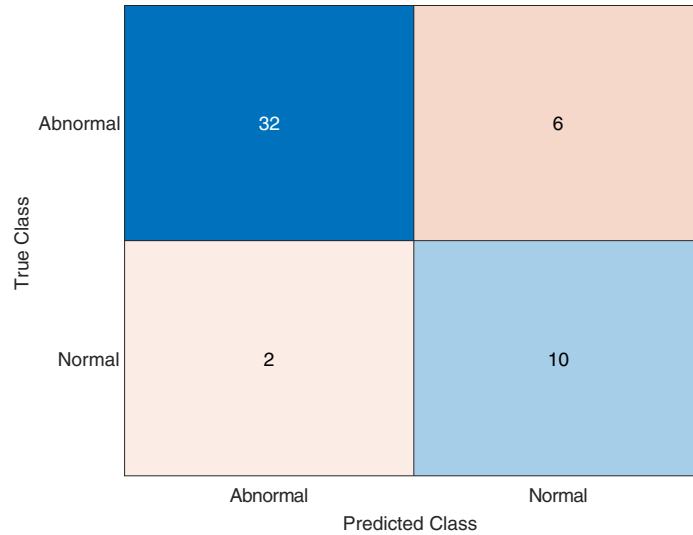


**Figure 18:** Confusion matrix: model prediction vs. radiologist assessment.

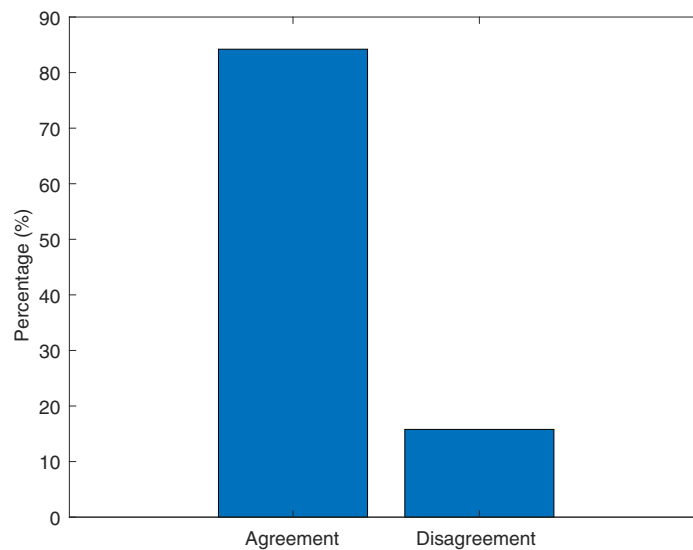


**Figure 19:** Agreement on abnormal cases.

### 9 Conclusion

The research presents a new fractional-order machine learning system that analyzes vertebral column defects through growth pattern analysis and abnormality prediction based on the UCI vertebral column dataset. The research introduces a unique approach to combine machine learning with fractional-order differential equations for simulating spinal tissue viscoelastic behavior, which depends on memory effects. The fractional derivative with optimized order  $\alpha = 0.8$  provides better disease progression modeling than integer-order models because it simulates long-term memory effects in biomechanical features like pelvic

incidence and lumbar lordosis angle, which creates a more accurate biological simulation of disease progression through pseudo-time sorting based on pelvic incidence. The method achieves high precision while showing understandable relationships between pelvic tilt and sacral slope through anatomical analysis, which produces a weighted mean squared error (MSE) of 0.0017 for normalized data fitting.

The strengths of this research are multifaceted. The machine learning component demonstrates robust performance, with Gradient Boost achieving the highest accuracy (0.937) and F1 score (0.829) across 10-fold cross-validation, outperforming benchmarks in classifying abnormal cases. Ensemble methods boost reliability through high AUC values, which reach 0.949 with Random Forest, and feature importance analysis shows that pelvic incidence plays a vital role in spinal alignment. The Banach fixed-point theorem, together with Lyapunov functions, provides theoretical proof that solutions exist and remain stable and bounded while accommodating negative coupling coefficients for biological inhibitory effects. The Adams-Bashforth-Moulton predictor-corrector method provides efficient numerical computation, and the developed GUI enables practical vertebral diagnosis applications that connect computational models to clinical practice. The research achieved various advancements, but certain limitations remained in the study. The dataset contains 310 instances, which were increased to 1000 through SMOTE, but this number might not represent all cases, especially for uncommon spinal conditions, and the model uses binary classification that combines different abnormalities into one category without separating tumor characteristics, which might reduce the accuracy of malignancy detection. The pseudo-time system functions as a disease severity indicator instead of tracking actual time progression, and the fixed fractional order  $\alpha$  fails to represent differences between patient groups and medical conditions.

The study relies on the UCI dataset with only 310 original instances, expanded to 1000 via SMOTE. While SMOTE mitigates class imbalance, synthetic data may introduce biases in pseudo-time analysis, potentially affecting the simulation of disease progression trajectories. Furthermore, the model may not generalize well to rare or severe cases, such as spinal fractures or deformities not represented in the dataset. Merging disk hernia and spondylolisthesis into a single 'abnormal' category simplifies binary classification but may obscure distinct pathological mechanisms, such as differing viscoelastic responses in each condition. Future studies should explore multi-classification models to differentiate these conditions and refine biomechanical simulations. Future validation on larger, diverse clinical datasets is recommended to assess robustness. The future development of this system requires expanding it to handle larger datasets from multiple centers, which will use imaging data to create actual 3D tumor models and perform real-time classification. The integration of adaptive fractional orders and hybrid models with deep learning systems will create more dynamic and precise results. The GUI needs to undergo clinical testing, which will determine its performance in actual medical environments. The current method can be applied to other musculoskeletal conditions and treatments, which will expand its reach to support personalized spinal care.

**Acknowledgement:** The authors gratefully acknowledge the support from the Mathematics Research Center at Near East University, INTI International University and the UCI Machine Learning Repository for providing the dataset.

**Funding Statement:** This research received no specific funding.

**Author Contributions:** David Amilo: conceptualization, methodology, software, formal analysis, investigation, data curation, writing, original draft preparation, writing, review and editing, and visualization. Khadijeh Sadri: conceptualization, formal analysis, investigation, writing, software, writing, review and editing, and visualization. Evren Hincal: methodology, investigation, resources, writing, review and editing, supervision, and project administration. Chinedu Izuchukwu: methodology, investigation, data curation, and writing, review and editing. Mohamed Hafez: investigation, writing, review and editing, supervision, and project administration. Muhammad Farman: validation, investigation, resources, writing, review and editing, and project administration. Kottakkaran Soopy Nisar:

validation, investigation, writing, review and editing, and supervision. All authors reviewed and approved the final version of the manuscript.

**Availability of Data and Materials:** The vertebral column dataset (specifically the file `column_2C.dat`) analyzed in this study is publicly available from the UCI Machine Learning Repository under a Creative Commons Attribution 4.0 International (CC BY 4.0) license. It can be accessed at <https://doi.org/10.24432/C5K89B> (Barreto, G., & Neto, A., 2005; also cited as reference [48] in this article). No additional data were generated or analyzed in this study.

**Ethics Approval:** This study is a secondary analysis of a publicly available, fully de-identified biomedical dataset. No new human participants or animal subjects were recruited or involved in any form of data collection, experimentation, or intervention for the present research. The dataset contains no identifiable personal information and is released under a Creative Commons Attribution 4.0 International (CC BY 4.0) license. Therefore, in accordance with standard institutional policies and international ethical guidelines, no institutional review board (IRB) approval or additional ethical clearance was required or obtained for this secondary analysis of publicly available, anonymized data.

**Conflicts of Interest:** The authors declare no conflicts of interest.

## References

1. Durbas A, Yilgor C, Alanay A. Functional anatomy of the spine. In: Sports injuries: prevention, diagnosis, treatment and rehabilitation. Cham, Switzerland: Springer Nature; 2025. p. 787–801. doi:10.1007/978-3-031-58351-3\_350.
2. Izzo R, Guarnieri G, Guglielmi G, Muto M. Biomechanics of the spine. Part I: spinal stability. *Eur J Radiol.* 2013;82(1):118–26. doi:10.1016/j.ejrad.2012.07.024.
3. Miele VJ, Panjabi MM, Benzel EC. Anatomy and biomechanics of the spinal column and cord. In: Handbook of clinical neurology. Vol. 109. Amsterdam, The Netherlands: Elsevier; 2012. p. 31–43. doi:10.1016/B978-0-444-52137-8.00002-4.
4. Enache AV, Toader C, Onciul R, Costin HP, Glavan LA, Covache-Busuioc RA, et al. Surgical stabilization of the spine: a clinical review of spinal fractures, spondylolisthesis, and instrumentation methods. *J Clin Med.* 2025;14(4):1124. doi:10.3390/jcm14041124.
5. Vendevre T, Germaneau A. Biomechanical insights and innovations in spinal pathology and surgical interventions. In: Spine surgery: general considerations and fundamental concepts. Vol. 1. Cham, Switzerland: Springer Nature; 2025. p. 47–62. doi:10.1007/978-3-031-85446-0\_4.
6. D'Aprile P, Tarantino A. Biomechanics of the spine. In: MRI of degenerative disease of the spine: a case-based atlas. Cham, Switzerland: Springer International Publishing; 2021. p. 3–9. doi:10.1007/978-3-030-73707-8\_1.
7. Sima S, Diwan A. Contemporary clinical perspectives on chronic low back pain: the biology, mechanics, etc. underpinning clinical and radiological evaluation. *JOR Spine.* 2025;8(1):e70021. doi:10.1002/jsp2.70021.
8. Adams MA. Biomechanics of back pain. *Acupunct Med.* 2004;22(4):178–88. doi:10.1136/aim.22.4.178.
9. Roussouly P, Pinheiro-Franco JL. Biomechanical analysis of the spino-pelvic organization and adaptation in pathology. *Eur Spine J.* 2011;20(Suppl 5):609. doi:10.1007/s00586-011-1928-x.
10. Shah A, Lemans JVC, Zavatsky J, Agarwal A, Krut MC, Matsumoto K, et al. Spinal balance/alignment—clinical relevance and biomechanics. *J Biomech Eng.* 2019;141(7):070805. doi:10.1115/1.4043650.
11. Kondratiev A, Smetankina N, Staude V. Biomechanical analysis of stress–strain distribution in the lumbar spine–sacrum–pelvis system with emphasis on sacroiliac joint dysfunction. *Prosthesis.* 2024;7(1):4. doi:10.3390/prosthesis7010004.
12. Backhaus JC, Jansen O, Kauczor HU, Sedaghat S. Fatty degeneration of the autochthonous muscles is significantly associated with incidental non-traumatic vertebral body fractures of the lower thoracic spine in elderly patients. *J Clin Med.* 2023;12(14):4565. doi:10.3390/jcm12144565.
13. Kim GU, Park WT, Chang MC, Lee GW. Diagnostic technology for spine pathology. *Asian Spine J.* 2022;16(5):764. doi:10.31616/asj.2022.0374.
14. Boraiah G, Chhabra A. Conventional and advanced imaging evaluation of spine. In: Multidisciplinary spine care. Cham, Switzerland: Springer International Publishing; 2022. p. 73–107. doi:10.1007/978-3-031-04990-3\_4.

15. Kim GU, Chang MC, Kim TU, Lee GW. Diagnostic modality in spine disease: a review. *Asian Spine J.* 2020;14(6):910. doi:10.31616/asj.2020.0593.
16. Mi Le JR, Yeh KT, Chen CW, Jaw FS, Yang SH, Wu WT. Quantitative evaluation of correlation between lumbosacral lordosis and pelvic incidence in standing position among asymptomatic Asian adults: a prospective study. *Sci Rep.* 2022;12(1):18965. doi:10.1038/s41598-022-21840-x.
17. Hey HWD, Tan JH, Ong B, Kumar A, Liu G, Wong HK. Pelvic and sacral morphology and their correlation with pelvic incidence, lumbar lordosis, and lumbar alignment changes between standing and sitting postures. *Clin Neurol Neurosurg.* 2021;211(2):107019. doi:10.1016/j.clineuro.2021.107019.
18. Hills J, Lenke LG, Sardar ZM, Le Huec J-C, Bourret S, Hasegawa K, et al. The T4-L1-hip axis: defining a normal sagittal spinal alignment. *Spine.* 2022;47(19):1399–406. doi:10.1097/BRS.0000000000004414.
19. Lahoti Y, Sai S, Ahmed W, Rajjoub R, Li M, Zaidat B, et al. Development of a novel machine learning model to automate vertebral column segmentation utilizing biplanar full-body imaging. *Spine J.* 2025;25(12):2803–10. doi:10.1016/j.spinee.2025.05.003.
20. Zhou S, Zhao Y, Sun Z, Han G, Zeng Y, Yu M, et al. Improving the accuracy of current sagittal alignment evaluation system centered around pelvic incidence: a new machine-learning based classification. *Eur Spine J.* 2025;35(1):84–94. doi:10.1007/s00586-025-08741-z.
21. Aleid AM, Alyabis NA, Almebki AA, Alshehri FD, Asiri AM, Almohsen Y, et al. Retrospective analysis of biomechanical features in orthopedic spine disorders: a study on predictive factors for spinal abnormalities. *J Med Life.* 2025;18(6):545–551. doi:10.25122/jml-2024-0336.
22. Magin RL. Fractional calculus in bioengineering: a tool to model complex dynamics. In: *Proceedings of the 13th International Carpathian Control Conference (ICCC); 2012 May 28–31; High Tatras, Slovakia.* p. 464–9. doi:10.1109/CarpathianCC.2012.6228688.
23. Magin R. Fractional calculus in bioengineering, part 1. *Crit Rev<sup>TM</sup> Biomed Eng.* 2004;32(1):1–104. doi:10.1615/CritRevBiomedEng.v32.i1.10.
24. Molinari L, Falcinelli C. On the human vertebra computational modeling: a literature review. *Meccanica.* 2022;57(3):599–622. doi:10.1007/s11012-021-01452-x.
25. Khan H, Alfwzan WF, Alzabut J, Almutairi DK, Azim MA, Thinakaran R. Artificial intelligence and neural networking for an analysis of fractal–fractional Zika virus model. *Fractals.* 2025;33(8):2540143. doi:10.1142/s0218348x25401437.
26. Amilo D, Sadri K, Farman M, Hafez M, Nisar KS, Izuchukwu RC. A hybrid fractional-order modeling and machine learning framework for cervical cancer prediction and dynamics. *Results Control Optim.* 2026;100689. doi:10.1016/j.rico.2026.100689.
27. Trachoo K, Chaiya I, Phakmee S, Prathumwan D. Dynamics of bone remodeling by using mathematical model under ABC time-fractional derivative. *Symmetry.* 2025;17(6):905. doi:10.3390/sym17060905.
28. Gabriel AT, Quaresma C, Vieira P. An innovative mathematical model of the spine: predicting Cobb and intervertebral angles using the 3D position of the spinous processes measured by vertebral metrics. *Algorithms.* 2024;17(4):134. doi:10.3390/a17040134.
29. Guo J, Yin Y, Peng G. Fractional-order viscoelastic model of musculoskeletal tissues: correlation with fractals. *Proc Royal Soc A.* 2021;477(2249):20200990. doi:10.1098/rspa.2020.0990.
30. Wang X, Guo J. Fractional-order viscoelastic model for tendons with multilevel self-similar structures. *Appl Math Model.* 2025;147:116222. doi:10.1016/j.apm.2025.116222.
31. Amilo D, Sadri K, Suleiman I, Farman M, Hincal E, Nisar KS. A study on fractional-order lung cancer model under different internal influences with time delays analysis and modeling. *Netw Model Anal Health Inform Bioinform.* 2025;14(66):1. doi:10.1007/s13721-025-00567-5.
32. Izuchukwu C, Amilo D, Sadri K, Yao HR, Yao JC. Application of a reflected forward-backward splitting method with momentum to a fractional-order lung cancer model. *Commun Nonlinear Sci Numer Simul.* 2025;14(1):18484. doi:10.1016/j.cnsns.2025.109055.
33. Amilo D, Sadri K, Hincal E. Malignant melanoma fractional-order mathematical model with stabilized fuzzy sliding mode control. *Comput Methods Programs Biomed.* 2025;270(4):108912. doi:10.1016/j.cmpb.2025.108912.

34. Gill AY, Saeed A, Rasool S, Husnain A, Hussain HK. Revolutionizing healthcare: how machine learning is transforming patient diagnoses-a comprehensive review of AI's impact on medical diagnosis. *J World Sci.* 2023;2(10):1638–52. doi:10.58344/jws.v2i10.449.
35. Asif S, Wenhui Y, ur-Rehman S, ul-ain Q, Amjad K, Yueyang Y, et al. Advancements and prospects of machine learning in medical diagnostics: unveiling the future of diagnostic precision. *Arch Comput Methods Eng.* 2025;32(2):853–83. doi:10.1007/s11831-024-10148-w.
36. Reyes SG, Bajaj PM, Herrera DE, Kurapaty SS, Chen A, Khazanchi R, et al. Predictive value of social determinants of health on 90-day readmission and health utilization following ACDF: a comparative analysis of XGBoost, random forest, Elastic-Net, SVR, and deep learning. *Global Spine J.* 2025;15(8):3797–806. doi:10.1177/21925682251332556.
37. Balaban B, Yilgor C, Yucekul A, Zulemyan T, Obeid I, Pizones J, et al. Building clinically actionable models for predicting mechanical complications in postoperatively well-aligned adult spinal deformity patients using XGBoost algorithm. *Inform Med Unlocked.* 2023;37(10193):101191. doi:10.1016/j.imu.2023.101191.
38. Haider M, Hashmi MSA, Raza A, Ibrahim M, Fitriyani NL, Syafrudin M, et al. Novel ensemble learning algorithm for early detection of lower back pain using spinal anomalies. *Mathematics.* 2024;12(13):1955. doi:10.3390/math12131955.
39. Mohammedqasim H, Mohammedqasem RA, Ata O, Alyasin EI. Diagnosing coronary artery disease on the basis of hard ensemble voting optimization. *Medicina.* 2022;58(12):1745. doi:10.3390/medicina58121745.
40. Akhtar T, Gilani SO, Mushtaq Z, Arif S, Jamil M, Ayaz Y, et al. Effective voting ensemble of homogenous ensembling with multiple attribute-selection approaches for improved identification of thyroid disorder. *Electronics.* 2021;10(23):3026. doi:10.3390/electronics10233026.
41. Zolfaghari B, Mirsadeghi L, Bibak K, Kavousi K. Cancer prognosis and diagnosis methods based on ensemble learning. *ACM Comput Surv.* 2023;55(12):1–34. doi:10.1145/3580218.
42. Ghadami A, Epureanu BI. Data-driven prediction in dynamical systems: recent developments. *Philosop Trans Royal Soc A.* 2022;380(2229):20210213. doi:10.1098/rsta.2021.0213.
43. de la Mata FF, Gijón A, Molina-Solana M, Gómez-Romero J. Physics-informed neural networks for data-driven simulation: advantages, limitations, and opportunities. *Phys A Stat Mech Appl.* 2023;610(7553):128415. doi:10.1016/j.physa.2022.128415.
44. Farea A, Yli-Harja O, Emmert-Streib F. Understanding physics-informed neural networks: techniques, applications, trends, and challenges. *AI.* 2024;5(3):1534–57. doi:10.3390/ai5030074.
45. Amilo D, Sadri K, Hincal E, Hafez M. A hybrid computational framework for Parkinson's disease prediction using fractional-order modeling and machine learning via vocal biomarkers. *Ain Shams Eng J.* 2026;17(1):103889. doi:10.1016/j.asej.2025.103889.
46. Amilo D, Sadri K, Hincal E. A hybrid approach to heart disease prediction using a fractional-order mathematical model and machine learning algorithm. *Comput Methods Biomech Biomed Eng.* 2025:1–30. doi:10.1080/10255842.2025.2523313.
47. Amilo D, Sadri K, Hincal E, Farman M, Nisar KS, Hafez M. An integrated machine learning and fractional calculus approach to predicting diabetes risk in women. *Healthc Anal.* 2025;8(2):100402. doi:10.1016/j.health.2025.100402.
48. Barreto G, Neto A. Vertebral column [Dataset]. UCI machine learning repository. [cited 2026 Mar 15]. Available from: <https://archive.ics.uci.edu/static/public/212/vertebral+column.zip>.
49. Abu-Shady M, Kaabar MK. A generalized definition of the fractional derivative with applications. *Math Probl Eng.* 2021;2021(1):9444803. doi:10.1155/2021/9444803.
50. Amilo D, Sadri K, Hincal E. Comparative analysis of caputo and variable-order fractional derivative algorithms across various applications. *Int J Appl Comput Math.* 2025;11(3):80. doi:10.1007/s40819-025-01887-w.
51. Ramesh K, Khan A, Abdeljawad T. Analysis of the stability of a predator-prey model including the memory effect, double Allee effect and Holling type-I functional response. *PLoS One.* 2025;20(1):e0305179. doi:10.1371/journal.pone.0305179.
52. Sousa IR, Nobrega KZ, Barreto GA. An analytical approach to the stability conditions of a new class of fractional-order control systems by the Lambert-Tsallis function. *IEEE Access.* 2024;12(1):175006–18. doi:10.1109/ACCESS.2024.3503562.